VITOR TAHA SANT'ANA

AERODYNAMIC MODELING USING NEURO-FUZZY FOR A SCALED MODEL OF CESSNA 182

UNIVERSIDADE FEDERAL DE UBERLÂNDIA
FACULDADE DE ENGENHARIA MECÂNICA
2019

VITOR TAHA SANT'ANA

AERODYNAMIC MODELING USING NEURO-FUZZY FOR A SCALED MODEL OF CESSNA 182

Master dissertation submitted to the Department of Mechanical Engineering – FEMEC-UFU, in partial fulfillment of the requirements for the degree of the Master Program in Mechanical Engineering. *EXAMINATION BOARD PRESENTATION COPY*

Concentration Area: Solid Mechanics and Vibrations

Advisor: Prof. Dr. Roberto Mendes Finzi Neto

Co-advisor: Prof. Dr. Tobias Morais

Uberlândia - MG

2019

Ficha Catalográfica Online do Sistema de Bibliotecas da UFU
com dados informados pelo(a) próprio(a) autor(a).

S231 Sant'Ana, Vitor Taha, 1994-
2019 MODELAGEM AERODINÂMICA UTILIZANDO NEURO-FUZZY PARA O AEROMODELO CESSNA 182 [recurso eletrônico] / Vitor Taha Sant'Ana. - 2019.

Orientador: Roberto Finzi.
Coorientador: Tobias Morais.
Dissertação (Mestrado) - Universidade Federal de Uberlândia, Pós-graduação em Engenharia Mecânica.
Modo de acesso: Internet.
Disponível em: http://dx.doi.org/10.14393/ufu.di.2019.2176
Inclui bibliografia.

1. Engenharia mecânica. I. Finzi, Roberto, 1974-, (Orient.). II. Morais, Tobias, 1981-, (Coorient.). III. Universidade Federal de Uberlândia. Pós-graduação em Engenharia Mecânica. IV. Título. CDU: 621

Bibliotecários responsáveis pela estrutura de acordo com o AACR2:
Gizele Cristine Nunes do Couto - CRB6/2091
Nelson Marcos Ferreira - CRB6/3074

UNIVERSIDADE FEDERAL DE UBERLÂNDIA

ATA DE DEFESA

Programa de Pós-Graduação ou Curso de Graduação em:	Engenharia Mecânica				
Defesa de:	Dissertação de Mestrado Acadêmico, nº 547, COPEM				
Data:	oito de agosto de dois mil e dezenove	Hora de início:	14:00	Hora de encerramento:	[17:12]
Matrícula do Discente:	11722EMC015				
Nome do Discente:	Vitor Taha Sant'ana				
Título do Trabalho:	Aerodynamic Modeling using Neuro-Fuzzy for a scaled model of Cessna 182				
Área de concentração:	Mecânica dos Sólidos e Vibrações				
Linha de pesquisa:	Dinâmica de Sistemas Mecânicos				
Projeto de Pesquisa de vinculação:					

Reuniu-se na sala de aula do LMEST, Bloco 1O, Campus Santa Mônica, da Universidade Federal de Uberlândia, a Banca Examinadora, designada pelo Colegiado do Programa de Pós-graduação em Engenharia Mecânica, assim composta: Professores Doutores: Rogério Sales Gonçalves - FEMEC/UFU; Daniel Alves Castello - COPPE/UFRJ; Roberto Mendes Finzi Neto - FEMEC/UFU; orientador(a) do(a) candidato(a).

Iniciando os trabalhos o(a) presidente da mesa, Dr(a). Roberto Mendes Finzi Neto, apresentou a Comissão Examinadora e o candidato(a), agradeceu a presença do público, e concedeu ao Discente a palavra para a exposição do seu trabalho. A duração da apresentação do Discente e o tempo de arguição e resposta foram conforme as normas do Programa de Pós-graduação em Engenharia Mecânica.

A seguir o senhor(a) presidente concedeu a palavra, pela ordem sucessivamente, aos(às) examinadores(as), que passaram a arguir o(a) candidato(a). Ultimada a arguição, que se desenvolveu dentro dos termos regimentais, a Banca, em sessão secreta, atribuiu o resultado final, considerando o(a) candidato(a):

Aprovado.

Esta defesa faz parte dos requisitos necessários à obtenção do título de Mestre.

O competente diploma será expedido após cumprimento dos demais requisitos, conforme as normas do Programa, a legislação pertinente e a regulamentação interna da UFU.

Nada mais havendo a tratar foram encerrados os trabalhos. Foi lavrada a presente ata que após lida e achada conforme foi assinada pela Banca Examinadora.

Documento assinado eletronicamente por **Roberto Mendes Finzi Neto**, **Professor(a) do Magistério Superior**, em 08/08/2019, às 17:11, conforme horário oficial de Brasília, com fundamento no art. 6º, § 1º, do Decreto nº 8.539, de 8 de outubro de 2015.

Documento assinado eletronicamente por **Rogerio Sales Gonçalves**, **Professor(a) do Magistério Superior**, em 08/08/2019, às 17:11, conforme horário oficial de Brasília, com fundamento no art. 6º, § 1º, do Decreto nº 8.539, de 8 de outubro de 2015.

Documento assinado eletronicamente por **DANIEL ALVES CASTELLO**, **Usuário Externo**, em 08/08/2019, às 17:13, conforme horário oficial de Brasília, com fundamento no art. 6º, § 1º, do Decreto nº 8.539, de 8 de outubro de 2015.

A autenticidade deste documento pode ser conferida no site https://www.sei.ufu.br/sei/controlador_externo.php?acao=documento_conferir&id_orgao_acesso_externo=0, informando o código verificador **1442272** e o código CRC **597DF592**.

VITOR TAHA SANT'ANA

MODELAGEM AERODINÂMICA UTILIZANDO NEURO-FUZZY PARA O AEROMODELO CESSNA 182

Dissertação apresentada à Faculdade de Engenharia Mecânica – FEMEC-UFU, como parte dos requisitos para obtenção do título de Mestre em Engenharia Mecânica. *EXEMPLAR DE DEFESA*

Área de Concentração: Mecânica dos Sólidos e Vibrações

Orientador: Prof. Dr. Roberto Mendes Finzi Neto

Coorientador: Prof. Dr. Tobias Morais

Uberlândia - MG

2019

To my family and friends for their unconditional love and support.

ACKNOWLEDGEMENTS

I would like to firstly thank my mom, my father and my brother, Leila, Mário and Felipe, for being my first school, teaching me the essential values in life: humility and respect. With their trust and full support, I could come this far, became an engineer and now, writing and researching to become a Master of Science.

I thank my laboratory friends, Felipe, Bruno, André and Higor which supported me till this moment, answering question and relieving the doubts during my journey. I also thank the friendship constructed during these short two years, with the students from post graduation program from the Faculty of Mechanical Engineering.

I also thank my first advisor, Prof. Dr. Leonardo Sanches to pointed me into the right direction, and to encouraged me many times. With his departure, Prof. Dr. Roberto Mendes Finzi Neto and Prof. Dr. Tobias Morais assumed the position of advisor and co-advisor, and they did it with mastery, they kept me in the right way till the end, helping me to solve every challenge found during the research, so I am very gratified to have had both on my side.

I would like to acknowledge the Federal University of Uberlândia, the Faculty of Mechanical Engineering and all professors that guided me during my graduation and post graduation. I thank the Graduate Program in Mechanical Engineering for the coordination of the course during these years.

I would like to acknowledge the Brazilian research agencies CAPES, CNPq and FAPEMIG for the financial support.

Lastly, but no least, I would also like to acknowledge the examination board for their patience reading this work and constructive critical approaches.

Thank the Gods for blessing and encouraging all this fantastic journey.

“O mais competente não discute,
domina a sua ciência e cala-se.”
(Voltaire)

“The most competent does not argue,
dominates his science and stay silent.”
(Voltaire)

RESUMO

SANT'ANA, V. T. **Modelagem aerodinâmica utilizando Neuro-Fuzzy para o aeromodelo Cessna 182**. 2019. 102 p. Dissertação (Mestrado em Engenharia Mecânica) – Faculdade de Engenharia Mecânica, Universidade Federal de Uberlândia, Uberlândia – MG, 2019.

Este trabalho tem o objetivo construir um modelo aerodinâmico, confiável, para um aeromodelo rádio controlado, uma réplica do Cessna 182 em escala. Para isso, foi utilizado a técnica de inteligência computacional conhecida como Neuro-Fuzzy, que pode ser interpretada como uma ferramenta capaz de imitar o comportamento de algum sistema após treinada. Os dados experimentais foram adquiridos através de uma placa de aquisição conhecida como Pixhawk-PX4. Após a aquisição dos dados, os mesmos foram divididos em duas categorias, o de treinamento e o de validação. Após a otimização feita pela Evolução Diferencial, para as funções de pertinência do Neuro-Fuzzy, com os dados de treinamento, o modelo foi capaz de prever as forças e os momentos para diferente atitudes do aeromodelo.

Palavras-chave: Neuro-Fuzzy, Evolução Direfencial, Aeromodelo, Pixhawk, Modelagem Aerodinâmica, Otimização, Cessna 182.

ABSTRACT

SANT'ANA, V. T. **Aerodynamic Modeling using Neuro-Fuzzy for a scaled model of Cessna 182**. 2019. 102 p. Dissertação (Mestrado em Engenharia Mecânica) – Faculdade de Engenharia Mecânica, Universidade Federal de Uberlândia, Uberlândia – MG, 2019.

This work has the main objective to obtain an aerodynamic model, as fidelity as possible, for an aircraft remote controlled, a replica of the Cessna 182 in scale. To conduct the idea, was used the computational intelligence technique known as Neuro-Fuzzy, which is capable of imitating the behavior of any system, if constructed with the help of a specialist. The experimental data were acquired through an acquisition board known as Pixhawk-PX4. After data acquisition, the same was divided into two parts, training and validation. After the optimization made by Neuro-Fuzzy, with the aid of a differential evolution for the training data, the model should be able to predict the forces and moments for different attitudes of the air model.

Keywords: Neuro-Fuzzy, Air model, Pixhawk, Aerodynamic Modelling, Optimization, Cessna 182.

LIST OF FIGURES

LIST OF TABLES

LIST OF ABBREVIATIONS AND ACRONYMS

ANFIS	Adaptive Network-based Fuzzy Inference System
ANN	Artificial Neural Networks
ARL	Army Research Laboratory
ARMA	AutoRegressive Moving Average Approach
CFD	Computational Fluid Dynamics
FDR	Flight Data Recorder
FFNN	Forward Fed Neural Network
FIS	Fuzzy Inference System
GNBR	Algorithm of Gauss-Newton approximation to Bayesian Regularization
IMU	Inertial Measurement Unit
MISO	Multi-Input Single-Output
NARX	Nonlinear AutoRegressive model with eXogenous variables
NED	North-East-Down
PCC	Pearson's correlation coefficient
RNN	Recent Neural Network
SRM	Structural Risk Minimization

LIST OF SYMBOLS

a_x — Acceleration in X axis direction

a_y — Acceleration in Y axis direction

a_z — Acceleration in Z axis direction

$\overline{c}$ — Mean aerodynamic chord

b — Wing Span

C_D — Drag coefficient force

$C_{D_{induced}}$ — Induced drag coefficient force

C_{D_0} — Parasite drag coefficient force

$C_{D_{wave}}$ — Wave drag coefficient force

C_L — Lift coefficient force

C_l — Moment coefficient around X axis

C_m — Moment coefficient around Y axis

C_n — Moment coefficient around Z axis

C_x — Force coefficient for X axis

C_y — Force coefficient for Y axis

C_z — Force coefficient for Z axis

F_x — Aircraft body force in X axis

F_y — Aircraft body force in Y axis

F_z — Aircraft body force in Z axis

I_{xx} — Moment of inertia around X axis direction

I_{xy} — Product of inertia between X and Y axis direction

I_{yy} — Moment of inertia around Y axis direction

I_{zz} — Moment of inertia around Z axis direction

k_1 — Longitudinal reduced frequency

k_2 — Lateral-directional reduced frequency

L — Moment around X axis

M — Moment around Y axis

m — Aircraft mass

N — Moment around Z axis

P — Body-axis roll rate

Q — Body-axis pitch rate

R_{xy} — Pearson correlation coefficient

R — Body-axis yaw rate

$\dot{p}$ — Body-axis roll acceleration

$\dot{q}$ — Body-axis pitch acceleration

$\dot{r}$ — Body-axis yaw acceleration

S — Reference area

T — Thrust

u — Aircraft velocity in X axis direction

V — Total Wind velocity

v — Aircraft velocity in Y axis direction

w — Aircraft velocity in Z axis direction

X — Aircraft longitudinal axis

Y — Aircraft transversal axis

Z — Aircraft body fixed Z direction

α — Angle-of-attack

$\dot{\alpha}$ — Angle-of-attack rate

β — Sideslip angle

$\dot{\beta}$ — Sideslip angle rate

δ_a — Aileron deflection

δ_e — Elevator deflection

δ_f — Flap deflection

δ_r — Rudder deflection

δ_s — Stablizer deflection

δ_{sb} — Speed-brake deflection

θ — Pitch angle

$\dot{\theta}$ — Pitch angle rate

ρ — Specific air mass

ϕ — Roll angle

$\dot{\phi}$ — Roll angle rate

ψ — Yaw angle

$\dot{\psi}$ — Yaw angle rate

CONTENTS

CHAPTER

1

INTRODUCTION

The ambition for new technologies is a humanity ambition. For many years the human race has been trying new ideas to achieve another level of technology, always trying to copy the mother nature, in almost everything. For example, genetic algorithms are based on our genetic code, and how it evolves with the aid of mutations and cross-overs between two genes.

In this present master thesis, a logic that contradicts the idea of Boolean logic was presented, and it is known as fuzzy logic. The fuzzy logic assemble with a differential evolution, or any other optimization of the Fuzzy Inference System (FIS) parameters, is known as Adaptive Network-based Fuzzy Inference System (ANFIS) or simply as Neuro-Fuzzy (JANG, 1992).

The Neuro-Fuzzy technique works as a polynomial curve fit, adapts itself with the output curve through the correlation between the input variables with the output variable, in a Multi-Input Single-Output (MISO) system (JANG, 1992). With this characteristic, it is possible to understand the behavior of any dynamic system, which in this case, is an aerodynamic system.

The objective of this master thesis is, evaluate the Neuro-Fuzzy technique, with experimental and numerical data, to get as close as possible to the real aerodynamic model of an aircraft, which in this case is a Cessna 182 in scale.

After the model construct, with experimental and numerical data, both will be compared and a conclusion between the numerical method and the experimental acquisition board will be presented.

This methodology was proposed to ensure that the aerodynamic model will be as close to reality as possible, to further apply the intelligent control of the Cessna 182, applying the Neuro-Fuzzy technique with the real aerodynamic stability derivatives for the aircraft in question.

1.1 Document Structure

This document is structured, as follows:

- Chapter 2: it is presented various techniques to perform the aerodynamic model of an aircraft. Hence, it is exposed some critics about the methods, concluding which method is the best for the objectives of this work;
- Chapter 3: it is exposed all the theories applied in the aerodynamic model construction, including the flight dynamics mathematical equations, the FIS and Neuro-Fuzzy architecture and the differential evolution theory;
- Chapter 4: it is performed the step by step from the numerical and experimental data acquisition, and this chapter consists of the presentation of all necessary instruments used, including the software and hardware;
- Chapter 5: it is presented all the results from the training and from the validation of the Neuro-Fuzzy model with numerical data, applying a critical analyses;
- Chapter 6: it is presented all the results from the training and from the validation of the Neuro-Fuzzy model with experimental data, also the results are analyzed and compared with the numerical results;
- Chapter 7: it is presented the conclusions from the presented work, encompassing the expectations and the possible future works.

CHAPTER

2

STATE OF THE ART

This section aims to evaluate the main aerodynamic modeling methodologies in the literature using computational intelligence techniques based on machine learning. After the evaluation of some procedures of performing aerodynamic modeling, a justification about the chosen method will be performed. The Neuro-Fuzzy method will be presented in an explanatory and didactic way in the next chapter as the selected modeling approach.

2.1 AutoRegressive Moving Average Approach

This method applied to aerodynamic modeling was used by Xing, Wang and Zhu (2016) to find the aerodynamic forces and moments of a rocket, flying in a supersonic regime. Besides the nonlinear aerodynamics, the authors proposed to find the trajectory based on the parameters identified as well.

Initially, in order to validate the method created (ARMA), the authors performed several non-stationary simulations using CFD, with supersonic velocities, involving maneuvering cases with NACA0012 airfoil.

According to the authors, the mathematical logic for AutoRegressive Moving Average Approach (ARMA) is based on system identification technique for Multi - Input Multi - Output (MIMO), the mathematical model structure can be expressed as:

$$y(k) = \sum_{i=1}^{n_a} A_i.y(k-i) + \sum_{i=0}^{n_b-1} B_i.u(k-i) \tag{2.1}$$

Where $y(k)$ is the aerodynamic force vector of step k, n_a and n_b are the output and input delay order, respectively, and $u(k-i)$ is the system input parameters. Following the equation, A_i and B_i are correlation matrices which bound the input to the output variables.

Following the authors reasoning, that the vector $S^n = (u^n v^n w^n \psi^n \phi^n \theta^n P^n Q^n R^n)$ is the

input variables vector, the Eq. 2.1 can be rewritten as:

$$F^n = \sum_{i=1}^{3} A_{n-i}.F^{n-i} + \sum_{i=0}^{2} B_{n-i}.S^{n-i} \tag{2.2}$$

Equation 2.2 may be rewriten in matricial form as presented in Eq. 2.3.

$$\begin{pmatrix} F^1 & F^2 & F^3 & S^2_{1X9} & S^3_{1X9} & S^4_{1X9} \\ F^2 & F^3 & F^4 & S^3_{1X9} & S^4_{1X9} & S^5_{1X9} \\ \dots & \dots & \dots & \dots & \dots & \dots \\ F^{n-3} & F^{n-2} & F^{n-1} & S^{n-2}_{1X9} & S^{n-1}_{1X9} & S^n_{1X9} \end{pmatrix} \cdot \begin{pmatrix} A_1 \\ A_2 \\ A_3 \\ B_{0_{1X9}} \\ B_{1_{1X9}} \\ B_{2_{1X9}} \end{pmatrix} = \begin{pmatrix} F^4 \\ F^5 \\ \dots \\ F^n \end{pmatrix} \tag{2.3}$$

The dimension number n depends on the number of chosen sample points, also the vectors F^n are the output forces.

To evaluate and validate this modeling approach, Xing, Wang and Zhu (2016) tested the NACA0012 airfoil in a range of training maneuvers cases, and the aerodynamic loads were obtained from Computational Fluid Dynamics (CFD) computation and from ARMA methodology for the comparison, resulting in a good convergence between both techniques, as presented in Fig. 1.

Figure 1 – Single degree of freedom lift coefficient comparison.

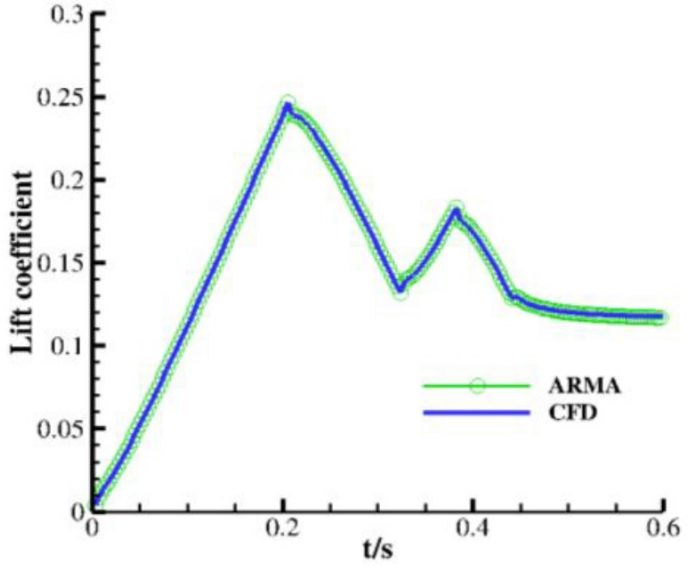

Source: Xing, Wang and Zhu (2016).

After the validation of the ARMA model, Xing, Wang and Zhu (2016) applied the technique in flight trajectory simulation of a rocket. The spinning projectile used was a missile from U.S.Army Research Laboratory (ARL), which is an axis-symmetric, consequently the products of inertia $I_{xy} = I_{xz} = I_{yz} = 0$.

The comparison of the aerodynamic forces between the CFD model and the ARMA model from the spinning projectile shown to the author the great approximation that his model has. The initial simulation conditions is presented in Tab. 1, also the Fig. 2 shows the comparison from both methods, with the rigid-body dynamics coupled in the models.

Table 1 – Initial state of trajectory simulation.

Direction n	Position (m)	Velocity (m/s)	Euler Angle (rad)	Angular rate (rad/s)
X	4.593	1 030.81	2.051	2518.39
Y	-0.2	22.064	0.088	-52.802
Z	-0.159	86.278	-0.023	22.233

Source: Adapted from Xing, Wang and Zhu (2016).

Figure 2 – Comparison of aerodynamic forces and moments calculated from ARMA model and CFD model.

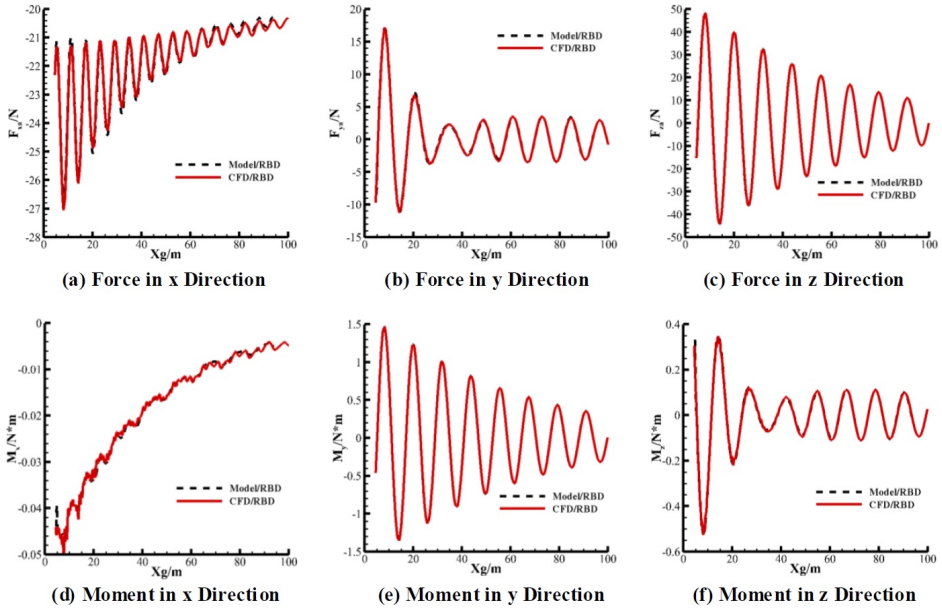

Source: Xing, Wang and Zhu (2016).

According to the authors conclusion, the ARMA model has the ability to substitute CFD simulations with the same accuracy and with low computational cost. They also affirms that, when the rigid-body dynamics equation are coupled with ARMA model, it is possible to predict the flight trajectory.

2.2 Supported Vector Machine

The Supported Vector Machine (SVM) is a statistical method which is capable to model nonlinear systems, and it was first developed for pattern identification in 1995, according to Wang, Qian and He (2015). This technique was applied in the unsteady aerodynamic modeling (WANG; QIAN; HE, 2015) with a large number of experimental data obtained in wind tunnel

tests and CFD simulations. To conduct to unsteady aerodynamics study, some maneuvers at high angles of attack were done with the aircraft used in the experiment.

The authors state that SVM exhibits more excellent empirical performance than Fuzzy Logics and Neural Networks, due the fact that SVM works with a statistical learning strategy, which takes into account the Structural Risk Minimization (SRM) principle.

The authors state that this is the first SVM approach applied to model high angle-of-attack unsteady aerodynamics, and it is the only work that was found in the bibliography review till the publish date.

An error minimization was applied in the SVM, the least squared (LS) minimization, transforming the method into LS-SVM. The authors selected some input variables according to his bibliography, for pitching oscillations the author selected the following variables as input $(\alpha, \dot{\alpha}, \ddot{\alpha}, k, \beta, \delta_e)$, in which α is the angle-of-attack, k is the reduced frequency, β is the sideslip angle and δ_e is the elevator deflection, and for yawing and rolling oscillations they took $(\alpha,\phi,\dot{\phi},k,\beta,\psi,\dot{\psi})$, in which ϕ is the roll angle and ψ is the yaw angle.

The results showed a great adaptability between the optimization and the experimental results for a delta wing aircraft at high angles of attack and different reduced frequencies (k).

Looking at the Fig. 3 it is evident that the curves starts to be nonlinear near the stall angle, where the aircraft partially loses the lift force due the discharge of the flow by increasing the angle of attack, in this condition the reduction of the angle generates an hysteresis effect due the non-linear condition.

The paper has a great problem approach and a good solution way, but it is not very clear within the equations and is the unique to apply the SVM technique in the aerodynamic modeling found in the literature.

2.3 Artificial Neural Network

In this section, some works with Artificial Neural Networks (ANN) application will be presented, especially in the aeronautical science, most of them will present the efficiency and speed of this computational technique. The pioneer to apply the ANN in the aeronautical science was the work published by Rajkumar and Bardina (2002), which predicted the lift coefficient curve as function of the angle-of-attack ($C_l x \alpha$) of an airfoil, using only sparse data for steady aerodynamics.

To achieve good results, the authors adopted the angle of attack as input variable of the ANN model. Also, the authors used numerical simulations and wind-tunnel experiments to feed the neural network. Rajkumar and Bardina (2002) further argue that is a reliable and fast method of predicting complex aerodynamics coefficients for flight simulation. The content of the article is focused in ANN capacity to interpolate sparse data using a nonlinear fit curve, with few

Figure 3 – Delta Wing Aircraft Coefficients experimental evaluation using SVM.

(a) Drag Coefficient

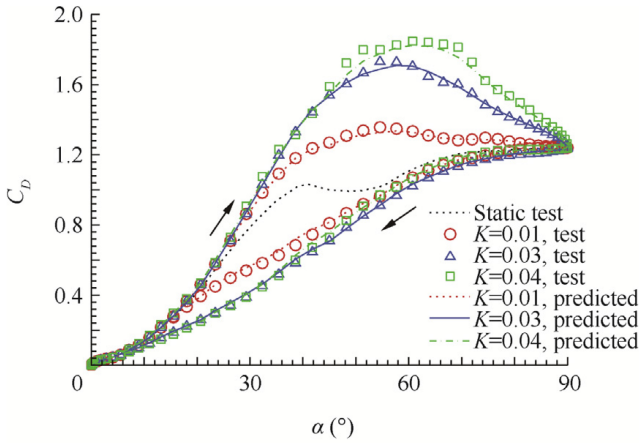

(b) Lift Coefficient

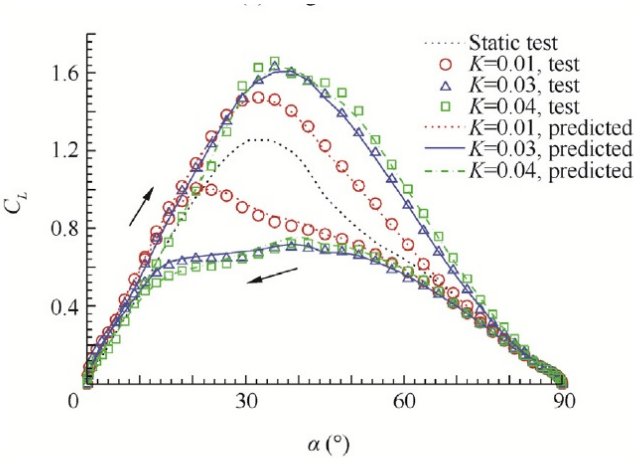

(c) Moment Coefficient

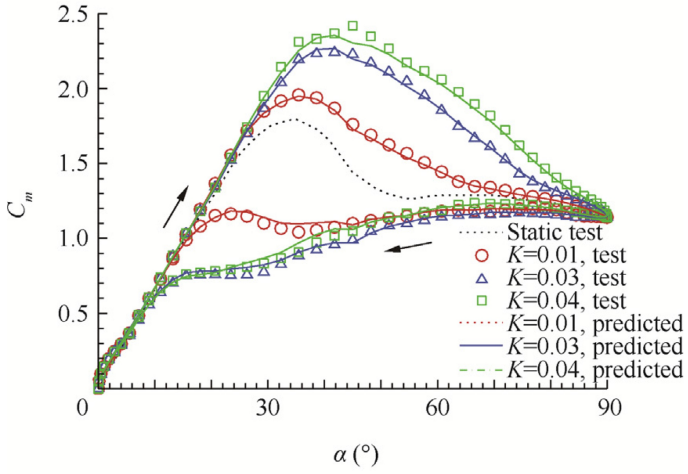

Source: Wang, Qian and He (2015).

experimental data. After the training process, the technique is capable to interpolate the linear and nonlinear relation between input and output variables.

To correlate the inputs with the outputs, the authors used the most effective variables for aerodynamics control, like angle-of-attack (α), sideslip angle (β), elevator deflection (δ_e), aileron deflection (δ_a), rudder deflection (δ_r), speed-break deflection (δ_{sb}), landing gear effects and ground effects. The input variables relate to force and moments equations on three body axis, defined by Roskam (1998). The input parameters vary according to Tab. 2.

Table 2 – Range of values involved in aerodynamics coefficients

Parameters	Ranges of values
Angle of attack (degrees)	$-10 < \alpha < 50$
Side angle (degrees)	$-20 < \beta < 20$
Mach number	$M \leq 0.9$
Surface deflection (degrees)	$-15 < \delta$elevons (flaps) < 15 $-20 < \delta$rudder < 20 $-20 < \delta$ailerons < 20 $0 < \delta$speedbrake < 80

Source: Rajkumar and Bardina (2002).

Firstly the authors trained the Neural Network with the necessary amount of data for the learning process. After training, some sparse data were presented to the ANN, and the model interpolates the region between the points, covering all the interval shown in Fig. 4b. The training sequence for $Mach \leq 0.4$ and $Mach > 0.4$ are shown in Fig. 4 and Fig. 5.

The authors Rajkumar and Bardina (2002) state that Neural Networks are powerful and important tool that NASA could explore in the near future, because the technique will allow to move directly from wind tunnel tests to virtual flight simulations. Besides, the authors either state that an hybrid system using evolutionary theory and neural network could attain an efficient model to predict the aerodynamic variables.

That was the idea applied recently by Secco and Mattos (2017), which use ANN in the prediction of the aircraft aerodynamic coefficients and wing parameters, which are presented in Tab. 3. The authors fed the neural network with results obtained through CFD simulations. The back-propagation algorithm was applied in the training process and a different number of neurons were evaluated to minimize the regression error.

The authors used wind tunnel experimental data, Fluent (Navier-Stokes equations solver) and potential flow code to obtain information about the 40 input variables which describe the problem. The Tab. 3 shows all the input variables and the the respective boundaries for optimization.

Each aerodynamic coefficient model was designed with a custom architecture composed by two layers varying from 20 to 100 neurons in steps of 20 neurons, with exception of lift

Figure 4 – Training sequence presented by the authors for $Mach \leq 0.4$

(a) Initial training data for neural network ($Mach \leq 0.4$)

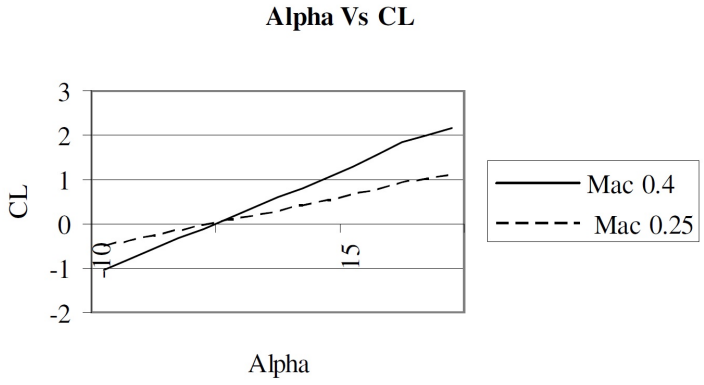

(b) Sparse data presented to neural network

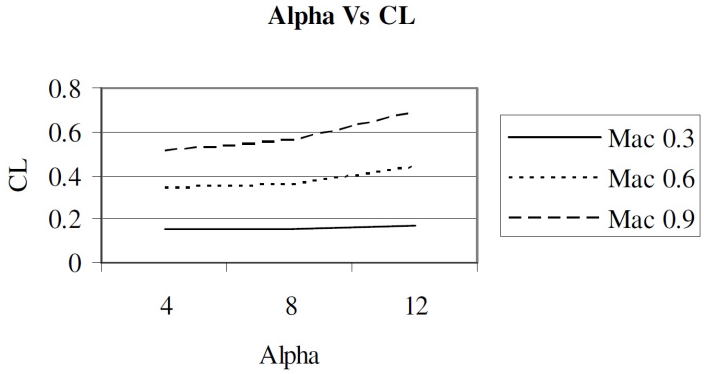

(c) Neural network interpolated data for sparse data ($Mach \leq 0.4$)

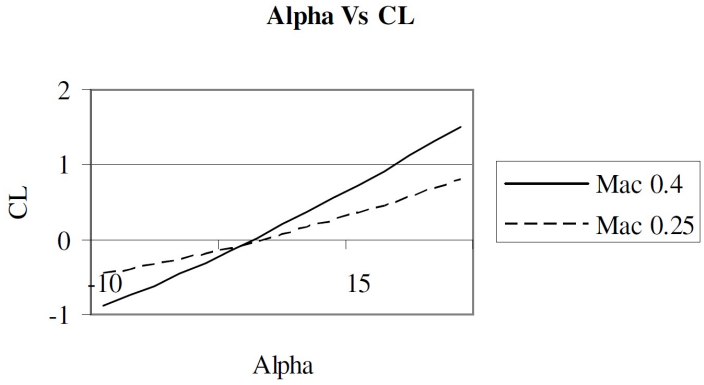

Source: Rajkumar and Bardina (2002).

coefficient, which could have an architecture varying from 20 to 160 neurons in the first layer, also varying in steps of 20 neurons.

After finding the best architecture for each aerodynamic coefficient, which are C_L (lift coefficient), $C_{D_{induced}}$ (induced drag coefficient), $C_{D_{wave}}$ (wave drag coefficient), C_{D_0} (parasite drag coefficient) and C_D (total drag coefficient), some wing parameters from Tab. 3 were separated and incorporated to obtain the trained ANN model. After the training, the ANN results were

Figure 5 – Training sequence presented by the authors for Mach > 0.4

(a) Initial training data for neural network ($Mach \geq 0.4$) (b) Neural network interpolated data for sparse data ($Mach \geq 0.4$)

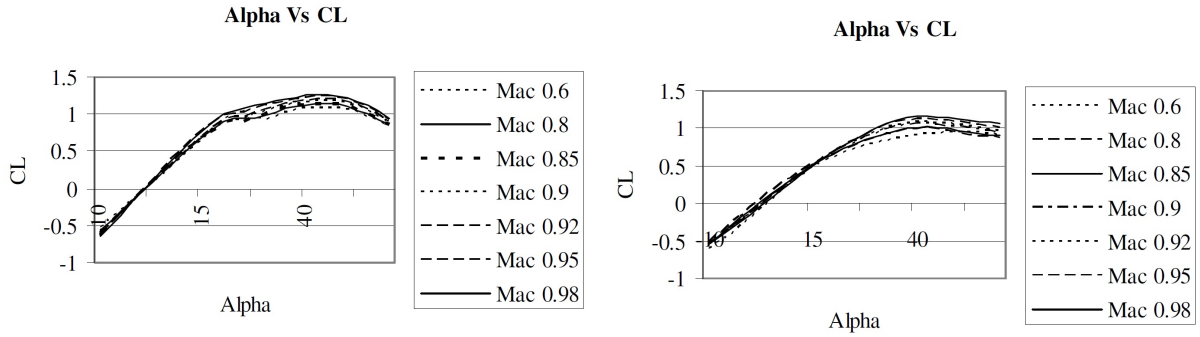

Source: Rajkumar and Bardina (2002).

compared with the CFD results, using two different sweep configurations, as Fig. 6 shows.

Figure 6 – Comparison between ANN predictions and CFD results for the baseline airplane with different wing sweep angles.

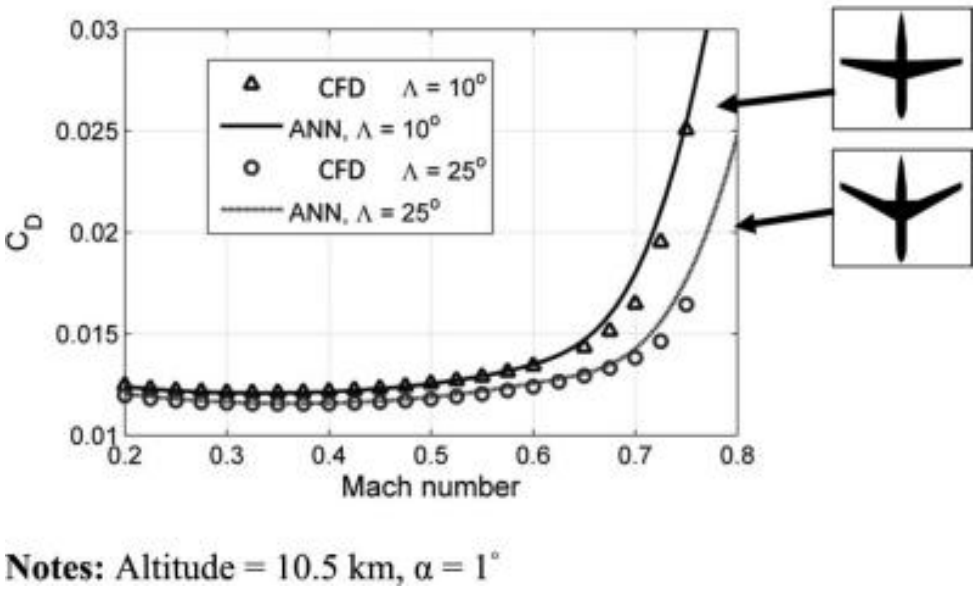

Source: Secco and Mattos (2017).

The authors exposed, in an evident way, that the computational cost from ANN tends to be much lower than the full potential code, and to prove that, they made a comparison between both methods, as shown in Tab. 4.

At the conclusion, the authors state that ANN is a surrogate model to replace a full-potential code in airplane MDO framework, they applied 100,000 cases to train and design the ANN, and they also showed that ANN is able to substitute CFD software to reduce the computational cost in a multidisciplinary optimization framework, with acceptable errors for conceptual design phase (SECCO; MATTOS, 2017).

Table 3 – Upper and lower boundaries for the ANN input variables

Variable	ID	Lower boundary	Upper boundary
Altitude	1	0	13,000 m
Mach number	2	0.2	0.8
Angle of attack	3	−3°	6°
Wing aspect ratio	4	7	11.5
Wing taper ratio	5	0.2	0.6
Wing leading-edge sweepback angle	6	10°	35°
Dihedral of the inboard wing	7	0°	5°
Dihedral of the outboard wing	8	0°	5°
Wing kink semi-span position (fraction of semi-span)	9	0.3	0.6
Wing area	10	50 m^2	200 m^2
Root airfoil incidence angle	11	0°	+3°
Kink airfoil incidence angle	12	−1°	+1°
Tip airfoil incidence angle	13	−3°	0°
Root airfoil parameters			
Leading edge radius (fraction of chord)	14	0.0050	0.20
Maximum relative thickness	15	0.10	0.16
Location of the maximum relative thickness	16	0.20	0.46
Camber where the maximum thickness is located	17	0.00	0.0025
Thickness line angle at trailing edge	18	−0.24	0.10
Camber line angle at leading edge	19	−0.20	0.10
Camber line angle at trailing edge	20	−0.30	−0.0050
Maximum camber	21	0.00	0.030
Maximum chamber location (fraction of chord)	22	0.50	0.80
Kink airfoil parameters			
Leading edge radius	23	0.003	0.20
Maximum relative thickness	24	0.080	0.125
Location of the maximum relative thickness	25	0.20	0.46
Camber where the maximum thickness is located	26	0.00	0.025
Thickness line angle at trailing edge	27	−0.24	0.10
Camber line angle at leading edge	28	−0.20	0.10
Camber line angle at trailing edge	29	−0.30	−0.0050
Maximum camber	30	0.00	0.030
Maximum chamber location (fraction of chord)	31	0.50	0.80
Tip Airfoil parameters			
Leading edge radius	32	0.003	0.15
Maximum relative thickness	33	0.080	0.12
Location of the maximum relative thickness	34	0.20	0.46
Camber where the maximum thickness is located	35	0.00	0.025
Thickness line angle at trailing edge	36	−0.24	0.10
Camber line angle at leading edge	37	−0.20	0.10
Camber line angle at trailing edge	38	−0.30	−0.0050
Maximum camber	39	0.00	0.030
Maximum chamber location (fraction of chord)	40	0.50	0.80

Source: Secco and Mattos (2017).

Another recent Neural Networks application was made by Ignatyev and Khrabrov (2015), which used different experiments to improve the model performance. This work focused on non linearity of unsteady aerodynamic characteristics, furthermore, the authors explored high-angle-of-attack simulations to predict non linearity on aerodynamic coefficients caused by the wing flow separation and reattachment, (IGNATYEV; KHRABROV, 2015).

Table 4 – Average CPU cost of each drag estimation methodology

Methodology	No. of evaluations	Overall processing time (s)	Average time (s)
Full Potential Code	8,000	174,788	21.8
ANN	8,000	44	0.0055

Source: Secco and Mattos (2017).

The work (IGNATYEV; KHRABROV, 2015) is focused on the pitching moment for an specific aircraft model, the Transonic CRuiser, which has high-sweep wing and canard configuration. The experiment set up performed in the wind tunnel were: V = 40 m/s, $\bar{c}$ = 0.2943 m, S = 0.3056 m^2, b = 0.3056 m.

The experiment was executed in three steps, the first was a static aircraft with the angles of attack varying between -10^o and 40^o at step of 2^o (A_0), the second experiment empowered to obtain the dynamic derivative of the angle of attack due a small oscillation amplitude, the dynamic derivative was calculated with the following equation:

$$\alpha = \alpha_0 + A_\alpha sin(2\pi ft + v_0) \tag{2.4}$$

$$\dot{\alpha} = 2\pi f A_\alpha cos(2\pi ft + v_0) \tag{2.5}$$

The amplitudes of oscillation were $A_\alpha = 10^o$ and 20^o for the dynamic experiment, and the frequencies were f = 0.5, 1.0 and 1.5 Hz (corresponding reduced frequencies $k = 2\pi f\bar{c}/2V$ = 0.012, 0.023 and 0.035). Ignatyev and Khrabrov (2015) identified a strong non-linear behavior in the aerodynamic derivatives for the following interval: $16^o < \alpha < 24^o$, being this region of non-linearity caused by the separation of the flow in the canard. For angles of attack above 24^o, the authors considered to be full developed and there are no significant dynamic contribution due to canard surface. Figure 7 compares the moment coefficient due the angle of attack results for the experimental and numerical simulations.

The authors considered two types of ANN architecture in his work. The first one is a Forward Fed Neural Network (FFNN) and Recent Neural Network (RNN), which was used to develop a model of unsteady pitch moment coefficient (IGNATYEV; KHRABROV, 2015). FFNN and RNN of Nonlinear AutoRegressive model with eXogenous variables (NARX) architecture is illustrated in the Fig. 8 below, which explain the working architecture.

In the training process, the author proposed the Bayes' rule to define the objective function parameters, to define the objective function F, that means they used an Algorithm of Gauss-Newton approximation to Bayesian Regularization (GNBR) for training ANN, once it is an effective tool to improve ANN generalization.

After the training procedure, the results were compared with the experimental data. The results obtained using the RNN architecture with NARX configuration is shown in Fig. 9.

Figure 7 – Comparison of the table model with the large amplitude oscillation experiments.

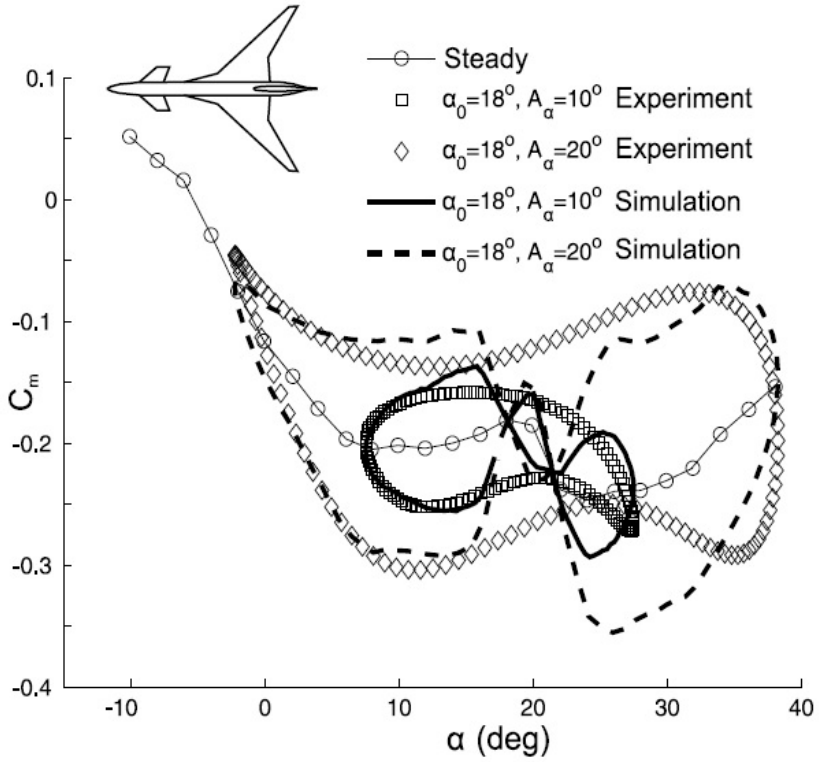

Source: Ignatyev and Khrabrov (2015).

After the comparative analysis of the methods for modeling the unsteady aerodynamic the authors concluded that the recurrent architectures were favorable for modeling of unsteady aerodynamic characteristics, also complement that RNN has better generalization ability, certifying that ANN methods are very interesting to model unsteady aerodynamics.

Every paper presented in this section applied the ANN approach in the aeronautical field, but none of them applied the technique to study experimentally the flight mechanics of an aircraft, which is the main objective of this master thesis. The ANN proved to be efficient in the unsteady aerodynamics flow studies, but not as much efficient as the Neuro-Fuzzy technique in the aerodynamic modeling of an aircraft with unknown aerodynamic characteristics.

2.4 Neuro-Fuzzy

This technique was first developed by Jang (1992), and almost two decades after his work, the researchers started to apply this methodology in aerodynamics modeling.

An interesting unsteady aerodynamic modeling using Neuro-Fuzzy were made by Chang (2013), which used a commercial aircraft equipped with a Flight Data Recorder (FDR) to record the main flight variables, like angle-of-attack, sideslip angle, the Euler angles and its derivatives, applying it to build a fuzzy logic-based aerodynamic model. Also, the methodology adopted by the author considered various triangular membership functions for the input variables.

Figure 8 – NN architectures; a) FFNN architecture; b) NARX architecture.

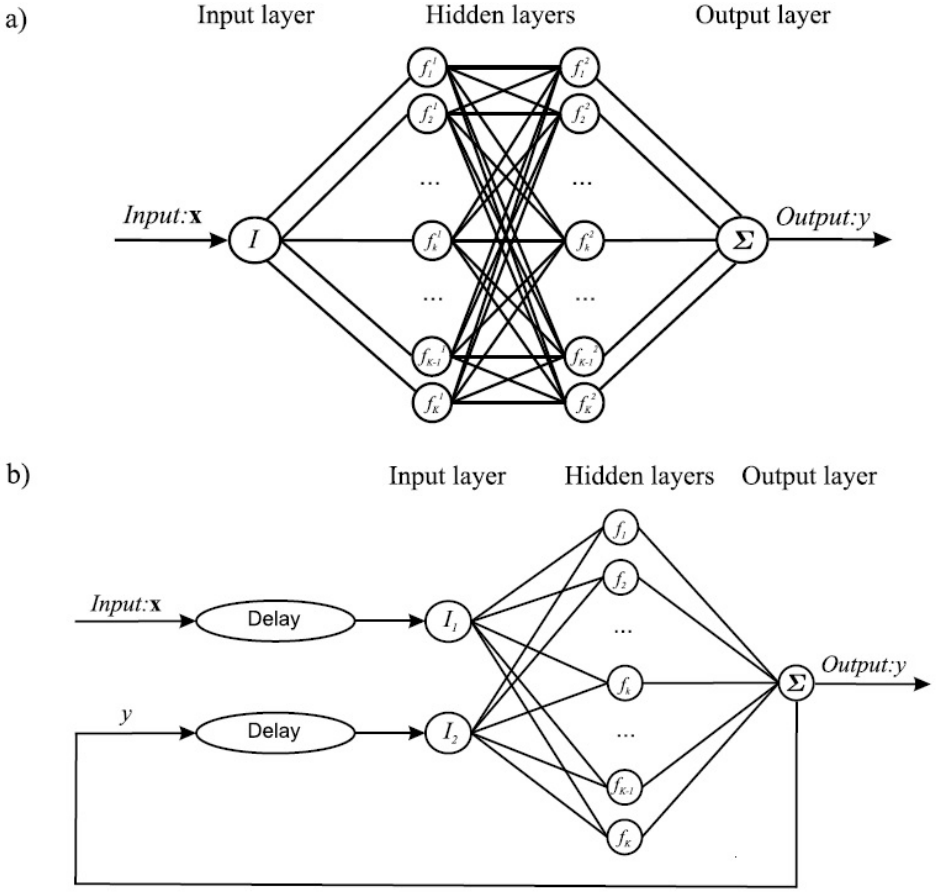

Source: Ignatyev and Khrabrov (2015).

The data was acquired during the flight with the help of FDR, and only a portion was applied in the Neuro-Fuzzy training process. The selected section include a clearly atmosphere perturbation (turbulence) during the transonic descent phase. The Fig. 10 shows this descent phase at a perturbed atmosphere with the altitude and angle-of-attack (α) variation.

The author choose to use, for the longitudinal aerodynamics, the following input variables to model the force and moments coefficients:

$$C_x, C_z, C_m = f(\alpha, \dot{\alpha}, Q, k_1, \beta, \delta_e, Ma, P, \delta_s, \bar{q}) \tag{2.6}$$

where the left hand represents the coefficients of the axial force (C_x), normal force (C_z) and pitching moment (C_m).

For the latero-directional aerodynamics, he chooses:

$$C_y, C_l, C_n = f(\alpha, \beta, \phi, P, R, k_2, \delta_a, \delta_r, Ma, \dot{\alpha}, \dot{\beta}) \tag{2.7}$$

Where the left hand represents the coefficients of the side force (C_y), rolling moment (C_l) and yawing moment (C_n).

Figure 9 – Unsteady aerodynamic derivatives of the pitch moment coefficient, simulated with RNN (lines) and obtained in the experiment (markers)

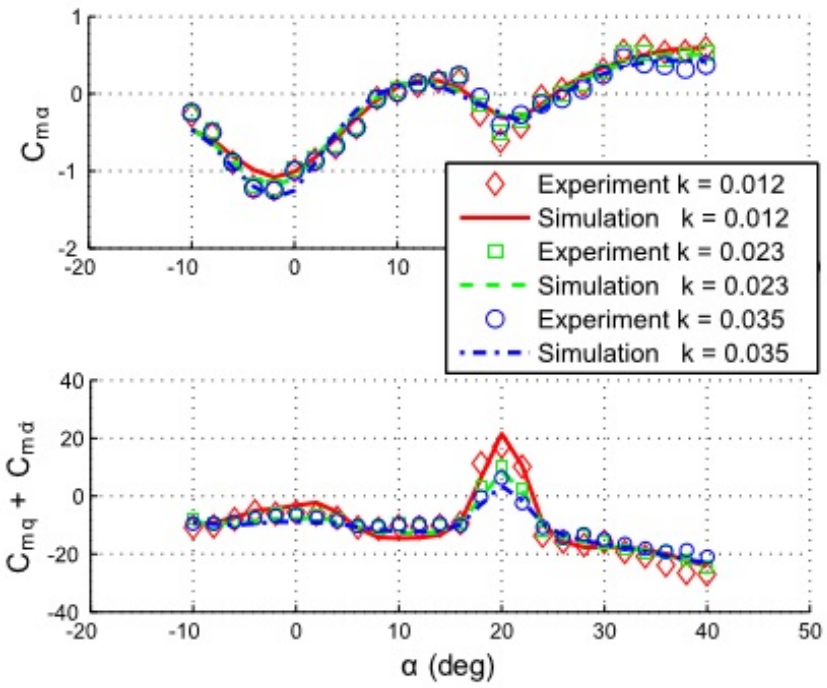

Source: Ignatyev and Khrabrov (2015).

After the training process, Chang (2013) determined the most important longitudinal and latero-directional static and oscillatory stability derivatives as a function of time. The Fig. 11 shows the main aircraft stability derivatives for force Z and moments M, L and N.

Chang (2013) concludes that the results could provide the understanding of the aerodynamic response of the analyzed aircraft in severe atmospheric turbulence. The author also states that the correlation between the input and output variables was improved by monitoring a multivariable correlation coefficient during the modeling process.

The main work which motivates to choose the Neuro-Fuzzy as tool to make the aerodynamic modeling of a Cessna 182 air model were presented by Brandon and Morelli (2012), and similar with Chang (2013) works, they used Neuro-Fuzzy to model unsteady aerodynamic, the first used advanced maneuvers during training data acquisition and second select a turbulent flight to do the training step.

The authors (BRANDON; MORELLI, 2012) tested airplane was an Aermacchi Impala MB-326M operated at the National Test Pilot School in Mojave CA to make the aerodynamic modeling with experimental data.

During the flight acquisition data, the authors aimed to achieve the biggest range of flight possibilities with several maneuvers, to include in the training process.

Brandon and Morelli (2012) carried out two interesting flight tests to understand better the aircraft dynamics and to acquire affinity with data acquisition system, they applied deflections

Figure 10 – The time history of flight variables in severe atmospheric turbulence during the descending phase in transonic flight.

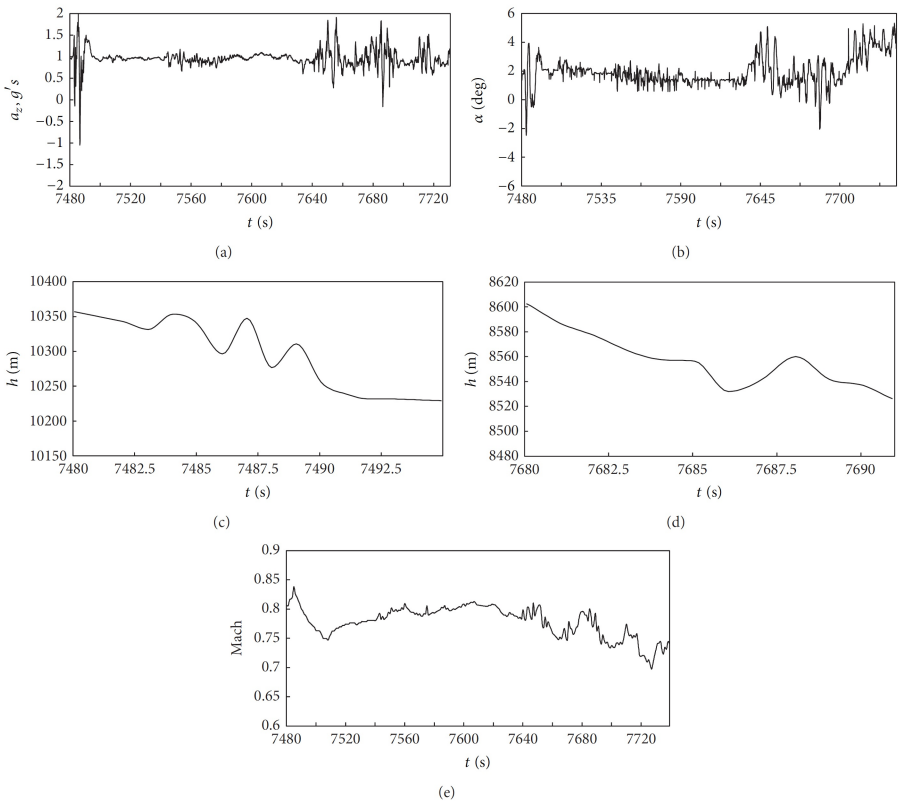

Source: Chang (2013).

Figure 11 – The time history of main longitudinal and latero-directional static stability derivatives along the flight path.

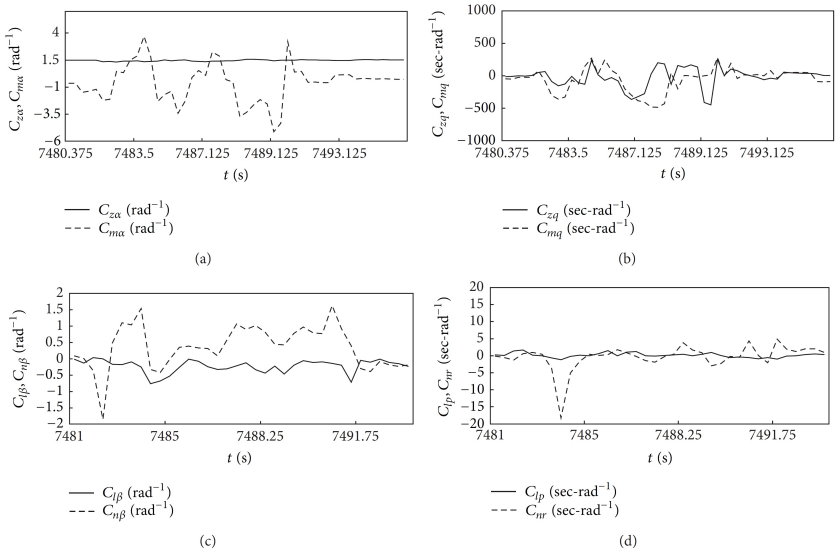

Source: Chang (2013).

of the three main command surfaces ($\delta_a, \delta_e, \delta_r$) one by one, that means, deflected the elevator alone, then deflected the rudder and later the aileron without moving any other control surface,

they called this process as "Doublets", then made all the surfaces deflecting simultaneously and randomly, denominating as "Fuzzy".

The input variables chosen to correlate with output variables were very similar with those selected by Chang (2013). The determining factor on the choice of the variables is called correlation factor (R^2), which express, through a number varying between 1 to 0, the correlation between the input and output variables, if the number is close to 1, means a high correlation, also if the number is close to 0, means a low correlation between the input and output. The Tab. 5 shows this correlation number between input and output variables.

Table 5 – Fuzzy Model Fit Quality with Combined Maneuvers

Coefficient	Correlation Coefficient, (R^2)	Explanatory Variables
C_x	0.983	$\alpha, \beta, \delta_e, \delta_a, \delta_r, \dot{\alpha}, \hat{p}, \hat{q}, \hat{r}$
C_y	0.967	$\alpha, \beta, \delta_e, \delta_a, \delta_r, \dot{\beta}, \hat{p}, \hat{q}, \hat{r}$
C_z	0.997	$\alpha, \beta, \delta_e, \delta_a, \delta_r, \dot{\alpha}, \hat{p}, \hat{q}, \hat{r}$
C_l	0.950	$\alpha, \beta, \delta_e, \delta_a, \delta_r, \dot{\beta}, \hat{p}, \hat{q}, \hat{r}$
C_m	0.971	$\alpha, \beta, \delta_e, \delta_a, \delta_r, \dot{\alpha}, \hat{p}, \hat{q}, \hat{r}$
C_n	0.964	$\alpha, \beta, \delta_e, \delta_a, \delta_r, \dot{\beta}, \hat{p}, \hat{q}, \hat{r}$

Source: Brandon and Morelli (2012).

Brandon and Morelli (2012) also could predict the hysteresis in the non-linear lift curve, as a result of the rich amount of data collected during the maneuvers, which possibly faced a stall condition, as shown in Fig. 12.

Figure 12 – Model fit to Normal force coefficient.

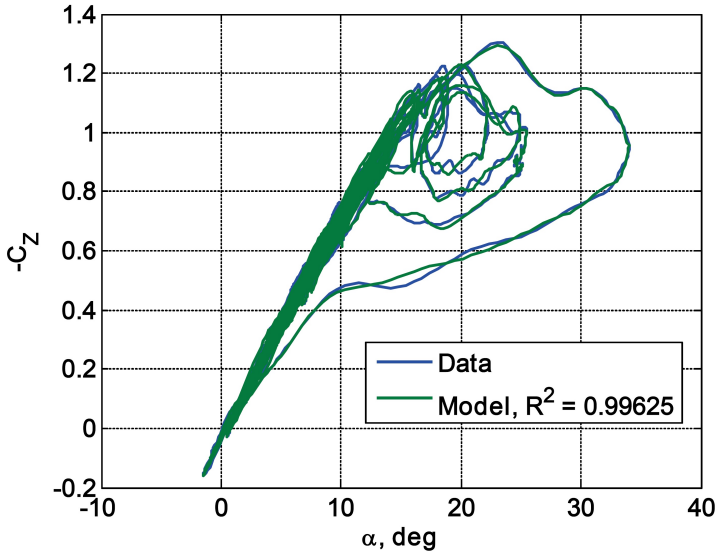

Source: Brandon and Morelli (2012).

One of the authors conclusion is the develop of a highly nonlinear aerodynamic model without knowing the aircraft structure model. Further, the authors state that fuzzy logic model results can be sensitive to explanatory variable selection and can also generate very nonlinear

results (BRANDON; MORELLI, 2012). Still, both authors warns that extrapolation of the model outside of data used to develop the model can result in unexpected results due to non-linearities.

2.5 Chapter Expectation

All of the articles presented in this section helped to choose which computational intelligence technique will take in considering in this work to accomplish the Cessna 182 aerodynamic model, and the work presented by Brandon and Morelli (2012) were the closest approach with the problem resolution. However, this present work will model an scaled aircraft, once Brandon and Morelli (2012) modeled a full scale aircraft, being this sentence the main difference between both works. Therefore, the Neuro-Fuzzy was chosen to be studied and applied in aerodynamic experimental model development.

The following chapters will perform the theoretical foundation, required to construct the aerodynamic model with experimental and numerical data.

CHAPTER

3

THEORETICAL FUNDAMENTATION

This chapter presents all theoretical substantiation that was necessary to understand the workings of the computational intelligence technique known as Neuro-Fuzzy, which uses an optimization to predict the best parameters of the membership functions. In addition, this chapter will also present the theory of flight mechanics, focusing on the relationship between inertial and non-inertial axes and how to transform one axis into another. Last but not least, the equation for rigid-body kinetics which describes the aircraft flight dynamic.

3.1 Adaptive Network-based Fuzzy Inference Systems

The ANFIS was first presented by Jang (1992) which combines the ability to correlate inputs with outputs from FIS with the learning and adaptation ability from ANN.

The ANFIS has the same structure in comparison with FIS, with "fuzzification" and "defuzzification" process combined with rule based to correlate input with outputs variables, as it can be seen in Pereira *et al.* (2017).

3.1.1 Fuzzy Inference System

The FIS is defined by 4 central steps: Input processor, rule based, inference machine and output processor (JAFELICE *et al.*, 2003), presented in Fig. 13 below.

The role of each FIS step is:

- **Input Processor (Fuzzification)**: Here occurs the translation of the input variables into Fuzzy sets in the respective domain. The presence of a specialist is fundamental to create the correct number of membership function to describe all the input domain.
- **Rule Based**: This component, combined with inference machine, could be considered the core of the Fuzzy Inference System. It is compound by many Fuzzy proposition of the

Figure 13 – Fuzzy Inference System architecture.

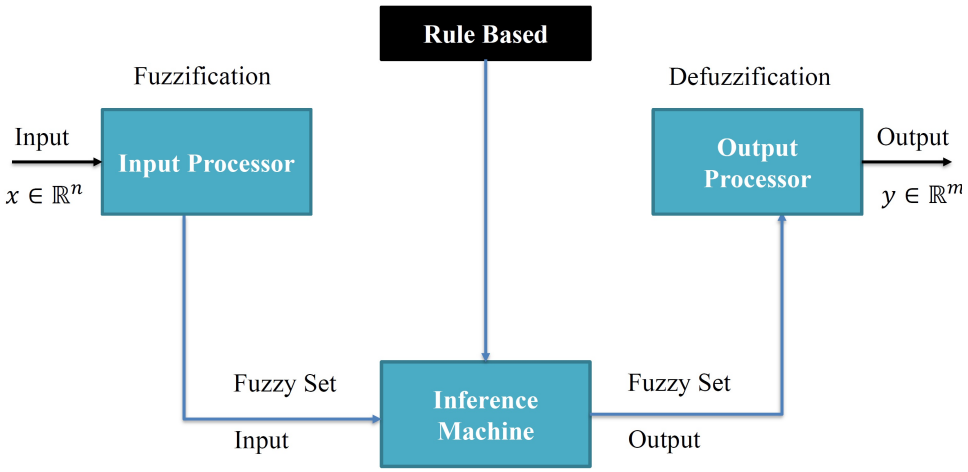

Source: Elaborated by the author.

type If...Then... Each proposition should be written with the help of a specialist knowledge. This step is responsible to describe all relations between the linguistic variables.

- **Inference Machine**: In this point, the Fuzzy prepositions are mathematically translated by means of the approximate reasoning. The mathematical operators are selected to define the Fuzzy relationship which models the rule based. Therefore, the inference machine is the most important step to ensure the correct work of the Fuzzy system, once it is in charge to provide the output for each input from the relation defined by the rule based. There are two main methods in the literature to make the relation: Mamdani Method and Takagi-Sugeno Method. The leading difference between both methods is the consequent type and the defuzzification proceeding.

  – **Mamdani Method**

  The Mamdani method combine the rules through a logic operator OR, which is modeled by the maximum operator and, in each rule, the logic operator AND is modeled by the minimum operator. Therefore, the rule based could be defined as:

  Rule 1: If (x is A_1 AND y is B_1) Then (z is C_1)

  Rule 2: If (x is A_2 AND y is B_2) Then (z is C_2)

  The output $z \in \mathbb{R}$ is obtained by the defuzzification of the output Fuzzy set $C = C'_1 \cup C'_2$ through the calculation of the centroid given by the union of the areas below the curve, as presented in Fig. 14.

  – **Takagi-Sugeno Method**

  In this method, the consequent is treated as a function of the input variables. For example, let suppose the function which characterizes the input and output of each rule be a linear combination of the inputs, that is, $z = px_1 + qx_2 + r$. Following the

Figure 14 – Mamdani Method.

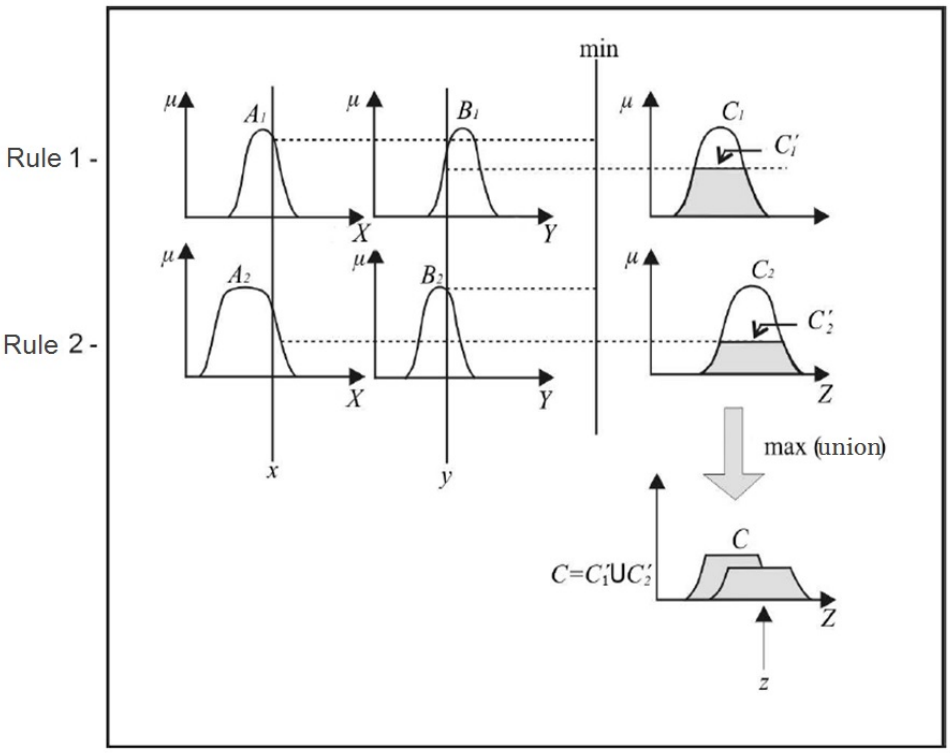

Source: Adapted from Jafelice *et al.* (2003).

same previous rule. Also, the Fig. 15 presents how the defuzzification is made by Takagi-Sugeno method.

Rule 1: If (x is A_1 AND y is B_1) Then (z is C_1)

Rule 2: If (x is A_2 AND y is B_2) Then (z is C_2)

The defuzzification is done, in Takagi-Sugeno's case, through the weighted average of the value of the degree of pertinence obtained from the rule base with the function that relates the input and output of the FIS.

- **Output Processor (Fuzzification)**: Here occurs the translation of a Fuzzy set into real number. Consequently, is necessary to choose one method to realize the output defuzzification to obtain a real number which represents the output Fuzzy set. The most comum method is the gravity center.

  – **Center of gravity**:

  This method is similar with the weighted average, with a singular difference which $C(z_i)$ is not the weight, is the compatibility degree for the value of z_i with the modeled concept of the Fuzzy set C.

  For a discreet domain:

$$G(C) = \frac{\sum_{i=0}^{n} u_i C(z_i)}{\sum_{i=0}^{n} C(z_i)} \tag{3.1}$$

Figure 15 – Takagi-Sugeno Method.

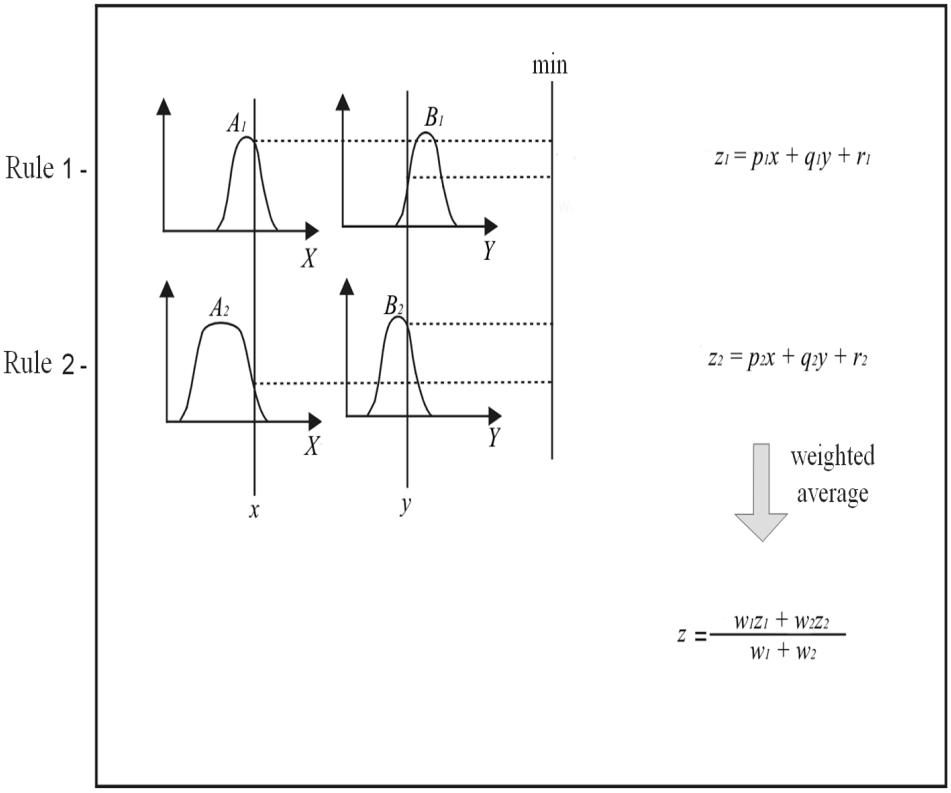

Source: Adapted from Jafelice *et al.* (2003).

For a continuous domain:

$$G(C) = \frac{\int_R u_i C(z_i)}{\int_R C(z_i)} \tag{3.2}$$

where R is the region of integration.

3.1.2 Neuro-Fuzzy

The Neuro-Fuzzy is derived from ANFIS, also developed by Jang (1992), and it consists by the FIS structure combined with the adaptation and learning ability of the ANN. The Neuro-Fuzzy architecture is presented in Fig. 16.

The purpose of each layer, using the Takagi-Sugeno inference is given by the the following definitions:

First Layer: Each node receives one input variables $I_i(k)$ that will be used in the training process. The output from i node from the first layer at time k, $u_i^{(1)}(k)$ is given by:

$$u_i^{(1)}(k) = I_i(k) \tag{3.3}$$

Second Layer: In this layer the fuzzification of input variables is performed, that is, the real numbers are transformed into Fuzzy subsets with a certain degree of pertinence. In this step, the membership functions (MF) are built for the description of the inputs. Considering that the

Figure 16 – Neuro-Fuzzy architecure representation.

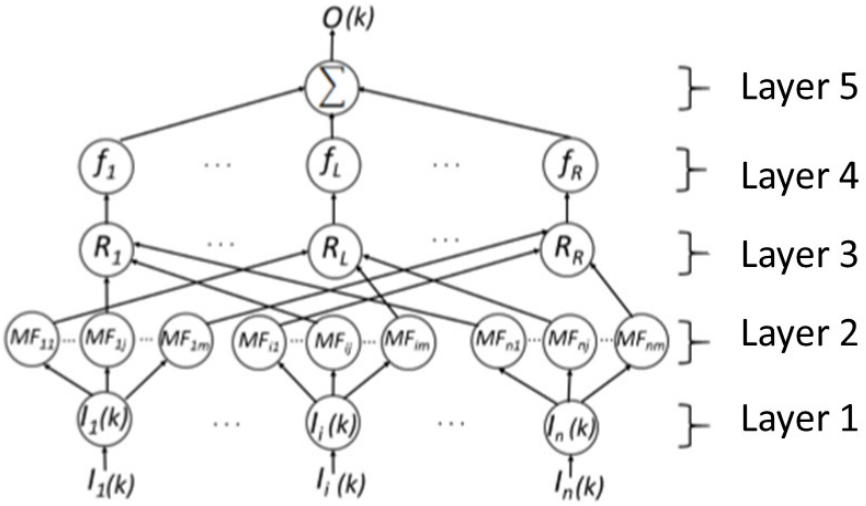

Source: Adapted from Pereira *et al.* (2017).

membership functions are approximated by gaussians, the output of node ij from layer 2 at time k, $u_{ij}^{(2)}(k)$, is given by:

$$u_{ij}^{(2)}(k) = e^{\frac{(u_i^{(1)}(k) - m_{ij}(k))^2}{\sigma_{ij}^2(k)}} \tag{3.4}$$

where $m_{ij}(k)$ e $_{ij}^{(2)}(k)$ are the mean and standard deviation, respectively, of the Gaussian membership function MF_{ij}.

Third Layer: Here the propositions of type If...Then... are realized, forming the rule based for ANFIS. For each rule, operator AND and OR are treated as minimum or maximum, respectively, so the output of the L node from this layer, $u_L^{(3)}(k)$, is a function of the layer 2 selected output from rule R_L.

Fourth Layer: The nodes from this layer are treated as constants, and are defined as a function $f_L : R^n \to R$ such that $f_L = f(I_1, ..., I_i, ..., I_n, w_{1L}, ..., w_{jL}, ..., w_{oL}, k)$, where $w_{1L}, ..., w_{jL}$, $..., w_{oL}$ are weights that will be determined in the ANFIS training phase. Thus the output from node L of layer 4, $u_L^{(4)}(k)$, is calculated by:

$$u_L^{(4)} = u_L^{(3)}(k) f_L(I_1, ..., I_i, ..., I_n, w_{1L}, ..., w_{jL}, ..., w_{oL}, k) \tag{3.5}$$

Fifth Layer: The last layer releases the ANFIS answer, given by equation:

$$O(k) = \frac{\sum_{L=1}^{R} u_L^{(4)}(k)}{\sum_{L=1}^{R} u_L^{(3)}(k)} \tag{3.6}$$

3.1.3 Differential Evolution

The optimization method used in this document was first developed by Storn and Price (1997), which is a minimization function method, it can be non-linear and non-differenciable, also is a faster heuristic optimization method with greater accuracy in comparison with other global optimization methods. This robust method requires few variables, and has a facility to be implemented, also has good adaptability to parallel computation, Storn and Price (1997).

The differential evolution method seek to find the minimum global from an objective function $F_{obj}(X)$, therefore is a heuristic method, differently from the classic optimization methods. It is important to know that X is a vector which the elements represent each optimization variable of interest.

According to Pereira *et al.* (2017), the differential evolution carries four important steps, as the Fig. 17 presents:

Figure 17 – Differential Evolution representation.

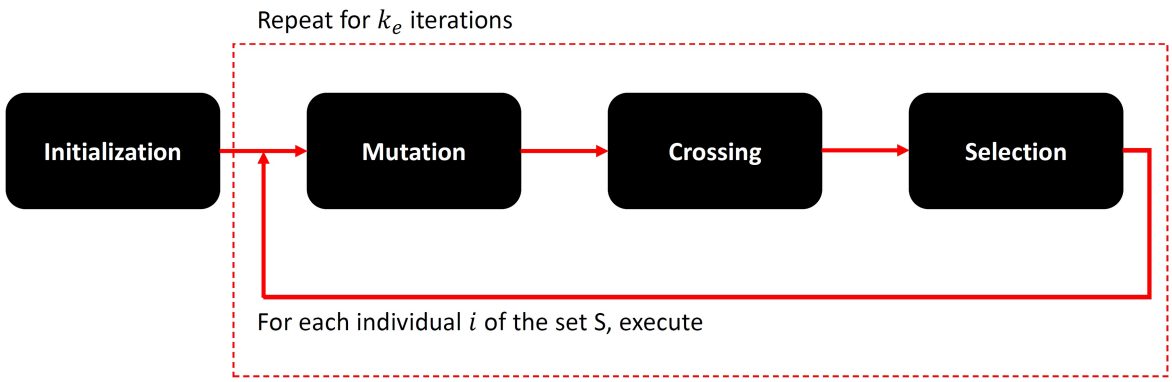

Source: Adapted from Pereira *et al.* (2017).

At the *initialization* of the optimization, all the useful parameters during the execution are set, also the limits of the variables of interest. Each individual is a vector $X_{i,0}$ which carries a possible result for the optimization and the aptitude with the objective function of each vector are calculated.

At the *mutation* phase, some alterations are made in the vectors $X_{i,k}$, according to the Eq. 3.7.

$$V_{i,k} = X_{i,k} + F(X_{j,k} - X_{l,k}) \tag{3.7}$$

In which $V_{i,k}$ is the resultant vector of the vector $X_{i,k}$ in the k iteration, F is the perturbation factor of vector $X_{i,k}$, generally between [0,2], $X_{j,k}$ and $X_{l,k}$ are vectors chosen aleatory that belong to the set (or population) S of the possible solutions. This process is repeated n times, in which n is the element number of the set S.

At the *crossing* stage, the information of the vector $V_{i,k}$ merges with the vector $X_{i,k}$, ensuring more diversification to the population. Each element e of the vector $V_{i,k}$ is associated with an aleatory number contained in the interval [0,1] (*rand(0,1)*) and is related with the value of the crossing rate (CR), also defined between the interval [0,1]. The decision is taken according to the Eq. 3.8.

$$C_{e,i,k} = \begin{cases} V_{e,i,k}, & \text{if } rand(0,1) \leq \text{OR } e = randnum(1,n_e) \\ X_{e,i,k}, & \text{if } rand(0,1) > \text{AND } e \neq randnum(1,n_e) \end{cases} \tag{3.8}$$

In which $C_{i,k}$ is the candidate vector to join in the set S in the iteration $k+1$ and $randnum(1,n_e)$, beeing n_e the number of vectors, is a integer organized number generator scattered in the interval $[1,n_e]$. This proceeding is repeated for all vectors inside the set S.

The *selection* is the last standard operator of the differential evolution and it is based in the analyses of the vectors $C_{i,k}$ generated in the crossing step. The Eq. 3.9 describes the selection proceeding, also made for all vectors in the set S. After the selection, the code return to the first step, *selection*, and the iteration advances to $k+1$ repeating all the process.

$$X_{i,k+1} = \begin{cases} X_{i,k}, & \text{if } f_{obj}(X_{i,k}) \leq f_{obj}(C_{i,k}) \\ C_{i,k}, & \text{if } f_{obj}(X_{i,k}) > f_{obj}(C_{i,k}) \end{cases} \tag{3.9}$$

Differential Evolution was used to predict the coefficients of the membership functions of the Fuzzy Inference System, that are the mean and the standard deviation from Gaussian curves, following the architecture of the Neuro-Fuzzy, which was explained in the subsection 3.1.2, the differential evolution optimize the second and the fourth layer.

In this presented work, the f_{obj} is given by:

$$C_f = \frac{\sum_{i=1}^{n} \sqrt{(\hat{y}_i - y_i)^2}}{n} \tag{3.10}$$

Where $\hat{y}_i$ is the Neuro-Fuzzy predicted result, y_i is the data value and n is the number of data points.

3.2 Aerodynamics Forces and Moments

First, it is necessary to understand the air craft body axes and its components (forces, moments and Euler angles). To better describe this coordination system, the Fig. 18 is presented.

This subsection presents a brief review about forces and moments in the aircraft body-axis and how to correlate with the wind-axis. According to Roskam (1998) there are two types of flight conditions: 1-) Steady state and 2-) Perturbed state.

Figure 18 – Definition of aircraft body axes, generalized velocities, forces, moments and Euler angles (Mclean 1990).

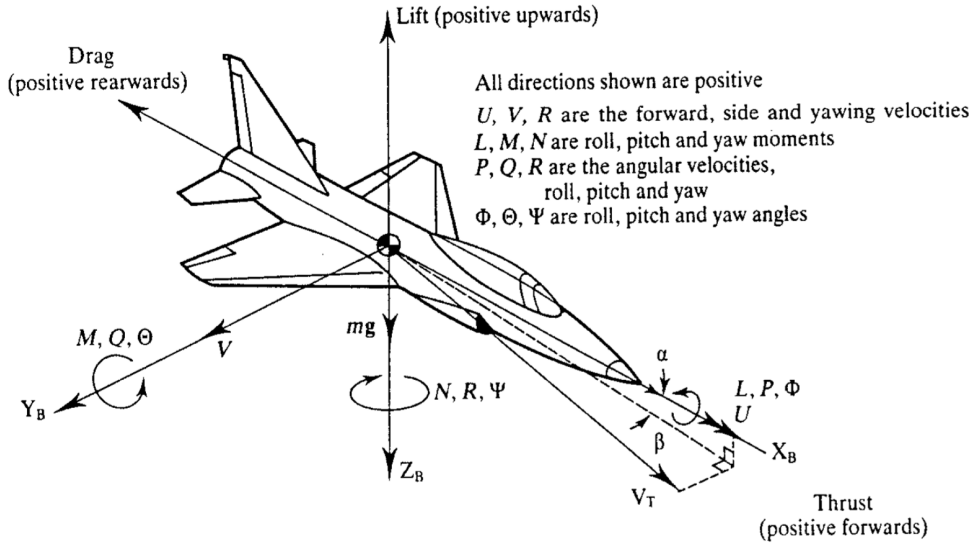

Source: Fossen (2011).

3.2.1 Steady State Flight

Steady state flight is a condition which the variables of motion does not varies through time. According with Roskam (1998) the most influential variables in the three body-axis forces and moments are described in the Tab. 6:

The steady state angular rates, P_1, Q_1 and R_1 are zero, that means the steady flight is a straight line flight condition.

In this case, the aerodynamic forces and moments for longitudinal body-axis is defined in Eq. 3.11 as:

$$\begin{aligned} F_x &= -D + T \\ F_z &= -L \\ M &= M \end{aligned} \tag{3.11}$$

And the Eq. 3.12 demonstrate the lateral-direction aerodynamic forces and moments

$$\begin{aligned} F_y &= S \\ L &= L \\ N &= N \end{aligned} \tag{3.12}$$

3.2.2 Perturbed Flight

According to Roskam (1998) each aircraft should have a different mathematical model, because they differ in configuration, shape and size. The approach made by Roskam (1998) is to first list the forces and moments to be modeled, then list all the variables of motion which

Table 6 – Dependence of Steady State Aerodynamic Forces and Moments of Variables.

Variable	All = 0	α	β	δ_a	δ_e	δ_r
F_{A_x}	Drag at zero values for all variable	Induced drag	Negligible for small: β	Negligible for small: δ_a	Negligible for small: δ_e	Negligible for small: δ_r
F_{A_y}	zero	Negligible for small: α	Side force due to: β	zero	zero	Side force due to: δ_r
F_{A_z}	Lift at zero values for all variable	Lift due to: α	Negligible for small: β	negligible	zero	negligible
L_A	zero	Rolling moment due to sideslip is affected by: α	Rolling moment due to: β	Rolling moment due to: δ_a	zero	Rolling moment due to: δ_r
M_A	Pitching moment at zero value for all variables	Pitching moment due to: α	Negligible for small: β	negligible	Pitching moment due to: δ_e	negligible
N_A	zero	Yawing moment due to sideslip is affected by: α	Yawing moment due to: β	Yawing moment due to: δ_a	zero	Yawing moment due to: δ_r

Source: Adapted from Roskam (1998).

experience shows to have a significant effect of the forces and moments. The Tab. 7 shows the most influent variables:

The structure of Tab. 7 is based on the following assumptions:

Table 7 – Dependence of Perturbed State Aerodynamic Forces and Moments on Variables.

Variable		F_X	F_Y	F_Z	L	M	N
Direct Variables	u	$\frac{\partial F_X}{\partial u}$		$\frac{\partial F_Z}{\partial u}$		$\frac{\partial M}{\partial u}$	
	v		$\frac{\partial F_Y}{\partial v}$		$\frac{\partial L}{\partial v}$		$\frac{\partial N}{\partial v}$
	w	$\frac{\partial F_X}{\partial w}$		$\frac{\partial F_Z}{\partial w}$		$\frac{\partial M}{\partial w}$	
	p		$\frac{\partial F_Y}{\partial p}$		$\frac{\partial L}{\partial p}$		$\frac{\partial N}{\partial p}$
	q	$\frac{\partial F_X}{\partial q}$		$\frac{\partial F_Z}{\partial q}$		$\frac{\partial M}{\partial q}$	
	r		$\frac{\partial F_Y}{\partial r}$		$\frac{\partial L}{\partial r}$		$\frac{\partial N}{\partial r}$
	$\dot{v}$		$\frac{\partial F_Y}{\partial \dot{v}}$		$\frac{\partial L}{\partial \dot{v}}$		$\frac{\partial N}{\partial \dot{v}}$
	$\dot{w}$	$\frac{\partial F_X}{\partial \dot{w}}$		$\frac{\partial F_Z}{\partial \dot{w}}$		$\frac{\partial M}{\partial \dot{w}}$	
Derived Variables	$\beta = \frac{v}{U_1}$		$\frac{\partial F_Y}{\partial \beta}$		$\frac{\partial L}{\partial \beta}$		$\frac{\partial N}{\partial \beta}$
	$\alpha \quad \frac{w}{U_1} = \alpha$	$\frac{\partial F_X}{\partial \alpha}$		$\frac{\partial F_Z}{\partial \alpha}$		$\frac{\partial M}{\partial \alpha}$	
	$\dot{\beta} = \frac{\dot{v}}{U_1}$		$\frac{\partial F_Y}{\partial \dot{\beta}}$		$\frac{\partial L}{\partial \dot{\beta}}$		$\frac{\partial N}{\partial \dot{\beta}}$
	$\dot{\alpha} = \frac{\dot{w}}{U_1}$	$\frac{\partial F_X}{\partial \dot{\alpha}}$		$\frac{\partial F_Z}{\partial \dot{\alpha}}$		$\frac{\partial M}{\partial \dot{\alpha}}$	
Control Variables	δ_a		$\frac{\partial F_Y}{\partial \delta_a}$		$\frac{\partial L}{\partial \delta_a}$		$\frac{\partial N}{\partial \delta_a}$
	δ_e	$\frac{\partial F_X}{\partial \delta_e}$		$\frac{\partial F_Z}{\partial \delta_e}$		$\frac{\partial M}{\partial \delta_e}$	
	δ_r		$\frac{\partial F_Y}{\partial \delta_r}$		$\frac{\partial L}{\partial \delta_r}$		$\frac{\partial N}{\partial \delta_r}$
	δ_f	$\frac{\partial F_X}{\partial \delta_f}$		$\frac{\partial F_Z}{\partial \delta_f}$		$\frac{\partial M}{\partial \delta_f}$	

Source: Adapted from Roskam (1998).

- Blanks indicate that a particular perturbed variable has NO effect on a particular perturbed force or moment.

- Partial derivatives indicate the slope by which a particular perturbed force or moment is affected by a particular perturbed variable.

This document will adopt the perturbed state flight to perform the unsteady aerodynamics model. The most influential variables in the forces and moments will be tested through the Pearson's correlation coefficient in Chapter 5.

3.2.3 Longitudinal

The airplane X force, which is expressed in Fig. 19, can be written as:

$$F_x = C_x \overline{q} S \tag{3.13}$$

Where C_X is the airplane X force coefficient, S is the wing reference area and $\overline{q}$ is the dynamic pressure. The total X force also depends on the Mach number, control surfaces deflections, airplane average skin friction coefficient and angle of attack, with that in mind, the X force coefficient equation for perturbed state flight could be written, according to Tab. 7, as:

$$C_x = C_{x_0} + C_{x_u} u + C_{x_w} w + C_{x_q} q + C_{x_{\dot{w}}} \dot{w} + C_{x_\alpha} \alpha + C_{x_{\dot{\alpha}}} \dot{\alpha} + C_{x_{\delta_e}} \delta_e + C_{x_{\delta_f}} \delta_f \tag{3.14}$$

Where the non-linear derivative coefficients are:

C_{x_0}	is the value of C_x for $\alpha = u = w = q = \dot{w} = \dot{\alpha} = \delta_e = \delta_f = 0$
$C_{x_u} = \partial C_x / \partial u$	is the change in airplane X force due to a change in X axis velocity.
$C_{x_w} = \partial C_x / \partial w$	is the change in airplane X force due to a change in Z axis velocity.
$C_{x_q} = \partial C_x / \partial q$	is the change in airplane X force due to a change in the pitch rate.
$C_{x_{\dot{w}}} = \partial C_x / \partial \dot{w}$	is the change in airplane X force due to a change in Z acceleration.
$C_{x_\alpha} = \partial C_x / \partial \alpha$	is the change in airplane X force due to a change in the angle-of-attack.
$C_{x_{\dot{\alpha}}} = \partial C_x / \partial \dot{\alpha}$	is the change in airplane X force due to a change in the angle-of-attack rate.
$C_{x_{\delta_e}} = \partial C_x / \partial \delta_e$	is the change in airplane X force due to a change in the elevator deflection.
$C_{x_{\delta_f}} = \partial C_x / \partial \delta_f$	is the change in airplane X force due to a change in the flap deflection.

The same reasoning is done for the Z force and the M moment. So the forces and moment in the longitudinal direction for the aircraft of interest can be written as:

$$F_x = -D = C_x \overline{q} S = (C_{x_0} + C_{x_u} u + C_{x_w} w + C_{x_q} q + C_{x_{\dot{w}}} \dot{w} + C_{x_\alpha} \alpha + C_{x_{\dot{\alpha}}} \dot{\alpha} + C_{x_{\delta_e}} \delta_e + C_{x_{\delta_f}} \delta_f) \overline{q} S \tag{3.15}$$

$$F_z = -L = C_z \overline{q} S = (C_{z_0} + C_{z_u} u + C_{z_w} w + C_{z_q} q + C_{z_{\dot{w}}} \dot{w} + C_{z_\alpha} \alpha + C_{z_{\dot{\alpha}}} \dot{\alpha} + C_{z_{\delta_e}} \delta_e + C_{z_{\delta_f}} \delta_f) \overline{q} S \tag{3.16}$$

$$M = C_m \overline{q} S \overline{c} = (C_{m_0} + C_{m_u} u + C_{m_w} w + C_{m_q} q + C_{m_{\dot{w}}} \dot{w} + C_{m_\alpha} \alpha + C_{m_{\dot{\alpha}}} \dot{\alpha} + C_{m_{\delta_e}} \delta_e + C_{m_{\delta_f}} \delta_f) \overline{q} S \overline{c} \tag{3.17}$$

3.2.4 Lateral-Directional

The airplane aerodynamic rolling moment is defined (ROSKAM, 1998) as:

$$L = C_l \overline{q} S b \tag{3.18}$$

Where C_l is the airplane rolling moment coefficient, S is the wing reference area, $\overline{q}$ is the dynamic pressure and b is the wing span. The total rolling moment also depends on the Mach number and Reynolds number, deflection of lateral control surfaces, deflection of directional control surfaces, sideslip angle and center of gravity location. With that in mind, the rolling moment coefficient equation for perturbed flight condition could be written as:

$$C_l = C_{l_0} + C_{l_v} v + C_{l_p} p + C_{l_r} r + C_{l_{\dot{v}}} \dot{v} + C_{l_\beta} \beta + C_{l_{\dot{\beta}}} \dot{\beta} + C_{l_{\delta_a}} \delta_a + C_{l_{\delta r}} \delta_r \tag{3.19}$$

Where the non-linear derivative coefficients are:

C_{l_0}	is the value of C_l for $\beta = v = p = r = \dot{v} = \dot{\beta} = \delta_a = \delta_r = 0$
$C_{l_v} = \partial C_l / \partial v$	is the change in airplane X moment due to a change in Y axis velocity.
$C_{l_p} = \partial C_l / \partial p$	is the change in airplane X moment due to a change in the roll rate.
$C_{l_r} = \partial C_l / \partial r$	is the change in airplane X moment due to a change in the yaw rate.
$C_{l_{\dot{v}}} = \partial C_l / \partial \dot{w}$	is the change in airplane X moment due to a change in Y acceleration.
$C_{l_\beta} = \partial C_l / \partial \beta$	is the change in airplane X moment due to a change in the sideslip angle.
$C_{l_{\dot{\beta}}} = \partial C_l / \partial \dot{\beta}$	is the change in airplane X moment due to a change in the sideslip angle rate.
$C_{l_{\delta a}} = \partial C_l / \partial \delta_a$	is the change in airplane X moment due to a change in the aileron deflection.
$C_{l_{\delta r}} = \partial C_l / \partial \delta_r$	is the change in airplane X moment due to a change in the rudder deflection.

Hence, similarly with the longitudinal equations, the force and moments for lateral-directional system can be written as:

$$L = C_l \overline{q} S b = (C_{l_0} + C_{l_v} v + C_{l_p} p + C_{l_r} r + C_{l_{\dot{v}}} \dot{v} + C_{l_\beta} \beta + C_{l_{\dot{\beta}}} \dot{\beta} + C_{l_{\delta_a}} \delta_a + C_{l_{\delta_r}} \delta_r) \overline{q} S b \tag{3.20}$$

$$F_y = C_S \overline{q} S = (C_{y_0} + C_{y_v} v + C_{y_p} p + C_{y_r} r + C_{y_{\dot{v}}} \dot{v} + C_{y_\beta} \beta + C_{y_{\dot{\beta}}} \dot{\beta} + C_{y_{\delta_a}} \delta_a + C_{y_{\delta_r}} \delta_r) \overline{q} S \tag{3.21}$$

$$N = C_n \overline{q} S b = (C_{n_0} + C_{n_v} v + C_{n_p} p + C_{n_r} r + C_{n_{\dot{v}}} \dot{v} + C_{n_\beta} \beta + C_{n_{\dot{\beta}}} \dot{\beta} + C_{n_{\delta_a}} \delta_a + C_{n_{\delta_r}} \delta_r) \overline{q} S b \tag{3.22}$$

3.2.5 Rotation matrices

According with Fossen (2011) there are three axes systems in the aircrafts in general:

- Body axis
- Stability axis
- Wind axis

Figure 19 – Cessna 182 three reference axis.

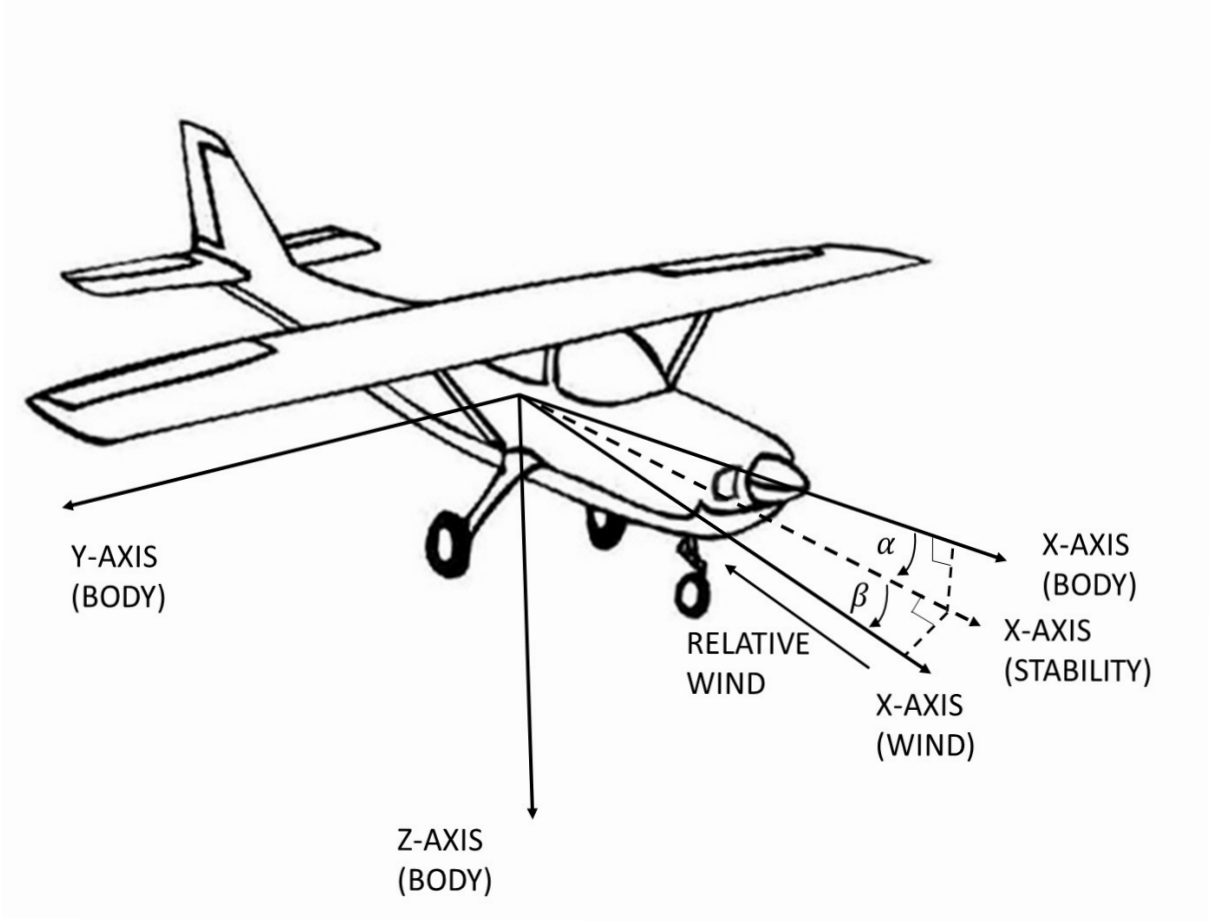

Source: Elaborated by the author.

The axes systems are shown in Fig 19 below where the angle of attack α and sideslip angle β are defined as:

$$\begin{aligned} tan(\alpha) &= \frac{W}{U} \\ sin(\beta) &= \frac{V}{V_T} \end{aligned} \tag{3.23}$$

where

$$V_T = \sqrt{U^2 + V^2 + W^2} \tag{3.24}$$

Finally, the rotation matrices for wind and stability axes could be defined according with Fossen (2011):

$$p^{wind} = R_{z,-\beta} p^{stab} = \begin{bmatrix} cos(\beta) & sin(\beta) & 0 \\ -sin(\beta) & cos(\beta) & 0 \\ 0 & 0 & 1 \end{bmatrix} p^{stab} \tag{3.25}$$

$$p^{stab} = R_{y,\alpha} p^{body} = \begin{bmatrix} cos(\alpha) & 0 & sin(\alpha) \\ 0 & 1 & 0 \\ -sin(\alpha) & 0 & cos(\alpha) \end{bmatrix} p^{body} \tag{3.26}$$

The rotation matrix becomes:

$$R^{wind}_{body} = R_{z,-\beta} R_{y,\alpha} \tag{3.27}$$

Hence:

$$p^{wind} = R^{wind}_{body} p^{body} \tag{3.28}$$

$$p^{wind} = \begin{bmatrix} cos(\beta) & sin(\beta) & 0 \\ -sin(\beta) & cos(\beta) & 0 \\ 0 & 0 & 1 \end{bmatrix} \begin{bmatrix} cos(\alpha) & 0 & sin(\alpha) \\ 0 & 1 & 0 \\ -sin(\alpha) & 0 & cos(\alpha) \end{bmatrix} p^{body} \tag{3.29}$$

$$p^{wind} = \begin{bmatrix} cos(\alpha)cos(\beta) & sin(\beta) & sin(\alpha)cos(\beta) \\ -cos(\alpha)sin(\beta) & cos(\beta) & -sin(\alpha)sin(\beta) \\ -sin(\alpha) & 0 & cos(\alpha) \end{bmatrix} p^{body} \tag{3.30}$$

This gives the following relationship between the velocities in body and wind axes:

$$v^{body} = \begin{bmatrix} U \\ V \\ W \end{bmatrix} = (R^{wind}_{body})^T v^{wind} = R^T_{y,\alpha} R^T_{z,-\beta} \begin{bmatrix} V_T \\ 0 \\ 0 \end{bmatrix} = \begin{bmatrix} V_T cos(\alpha)cos(\beta) \\ V_T sin(\beta) \\ V_T sin(\alpha)cos(\beta) \end{bmatrix} \tag{3.31}$$

The Eq. 3.31 above shows how to find the body-axis velocities from pitot tube velocity (V_T).

3.2.6 Rigid-body Kinetics

According with Fossen (2011), the aircraft rigid-body kinetics can be expressed as:

$$m(\dot{\nu_1} + \nu_2 x \nu_1) = \tau_1 \tag{3.32}$$

$$I_{CG}\dot{\nu_2} + \nu_2 x (I_{CG}\nu_2) = \tau_2 \tag{3.33}$$

Where $\nu_1 = [U,V,W]^T$, $\nu_2 = [P,Q,R]^T$, $\tau_1 = [X,Y,Z]^T$ and $\tau_2 = [L,M,N]^T$. It is assumed that the coordinate system is located in the aircraft center of gravity (CG). Therefore, the resulting model is written:

$$M_{RB}\dot{\nu}_1 + C_{RB}(\nu)\nu_1 = \tau_{RB} \tag{3.34}$$

Where

$$M_{RB} = \begin{bmatrix} mI_{3x3} & O_{3X3} \\ O_{3X3} & I_{CG} \end{bmatrix}, C_{RB}(\nu) = \begin{bmatrix} mS_{\nu_2} & O_{3X3} \\ O_{3X3} & -S(I_{CG}\nu_2) \end{bmatrix} \tag{3.35}$$

Where I_{3x3} is the identity matrix and O_{3x3} is a zero matriz. Also, the inertia tensor is defined as (assume that $I_{xy} = I_{yz} = 0$ which corresponds to xz plane of symmetry):

$$I_{CG} = \begin{bmatrix} I_X & 0 & -I_{XZ} \\ 0 & I_Y & 0 \\ -I_{XZ} & 0 & I_Z \end{bmatrix} \tag{3.36}$$

The forces and moments acting on the aircraft can be expressed according with Fossen (2011):

$$\tau_{RB} = -g(\eta) + \tau \tag{3.37}$$

Where τ is a generalized vector that includes aerodynamic and control forces. The gravitational force $f_G = \begin{bmatrix} 0 & 0 & mg \end{bmatrix}^T$ acts in the CG (origin of the body-fixed coordinate system) and this gives the following vector expressed in North-East-Down (NED) axis system:

$$g(\eta) = -(R^{ned}_{abc})^T \begin{bmatrix} f_G \\ O_{3X1} \end{bmatrix} = \begin{bmatrix} mgsin(\theta) \\ -mgcos(\theta)sin(\phi) \\ -mgcos(\theta)cos(\phi) \\ 0 \\ 0 \\ 0 \end{bmatrix} \tag{3.38}$$

Hence, the aircraft model can be written in matrix form as:

$$M_{RB}\dot{\nu}_1 + C_{RB}(\nu)\nu_1 + g(\eta) = \tau \tag{3.39}$$

Or in component form:

$$\begin{aligned} m(\dot{U} + QW - RV + gsin(\theta)) &= F_x \\ m(\dot{V} + UR - WP - gcos(\theta)sin(\phi)) &= F_y \\ m(\dot{W} + VP - QU - gcos(\theta)sin(\phi)) &= F_z \\ I_{xx}\dot{P} - I_{xz}(\dot{R} + PQ) + (I_{zz} - I_{yy})QR &= L \\ I_{yy}\dot{Q} - I_{xz}(P^2 - R^2) + (I_{xx} - I_{zz})PR &= M \\ I_{zz}\dot{R} - I_{xz}\dot{P} + (I_{yy} - I_{xx})PQ + I_{xz}QR &= N \end{aligned} \tag{3.40}$$

3.3 Chapter Expectation

With Eq. 3.40, all the forces and moments equations are exposed, and all the necessary theoretical foundation to elaborate a numerical and experimental Neuro-Fuzzy aerodynamic model for Cessna 182.

The following chapters will present how the numerical and experimental data was acquired. Also will present the treatment for experimental data.

CHAPTER

4

METHODOLOGY

The technique applied in this master thesis, to execute the aerodynamic modeling of the Cessna 182 scaled, is known as Neuro-Fuzzy. The data to feed the ANFIS was collected in two ways, first with the aid of XPLANE, a flight simulator certified by FAA. The second way, was during the flight of the scaled aircraft with the help of a data acquisition board known as Pixhawk PX4. The data was saved on a SD memory card and then imported into the Mission Planner software to be analyzed, later the data was imported into Matlab® and filtered to perform aerodynamic modeling with the aid of the developed model.

4.1 Cessna 182

The aircraft Cessna 182 Skylane is a very consecrated aircraft introduced in 1957 in the aircraft market. The land gear is a tricycle gear configuration and the aircraft has high wing configuration with a single piston powertrain, the motor model is a Lycoming O-540 air-cooled with 230 hp (170 kW). The Fig. 20 illustrate the real scale airplane, also the geometry configurations of the model airplane are defined according to Tab 8.

The scaled version of Cessna 182 is made by ART-TECH, and has the same geometry configuration as real scale Cessna 182, with exception of the powertrain, which in the scale version is an electric motor with 800 RPM/V produced by company itself (rotations per minute per volt). The Fig. 21 shows the model airplane disassembled.

All the aircraft geometries were measured or estimated, which was the case of the inertia moments, with the aid of the model aircraft designed in the XPLANE. The Tab. 8 shows the obtained values.

Figure 20 – Real scale Cessna 182.

Source: Aeronef.net (2019).

Figure 21 – Cessna 182 in scale (model airplane).

Source: Elaborated by the author.

Table 8 – Necessary geometric measurements for Cessna 182 model airplane.

Parameters	Value
Wing span, b [m]	1.3
Aspect ratio, $\mathcal{AR}$ [-]	7.4
Mean aerodynamic chord, $\overline{c}$ [m]	0.177
Mass, m [kg]	1.5
Wing area, S [m^2]	0.228
Inertia moments, I_{xx}, I_{yy}, I_{zz} [kg.m^2]	0.05, 0.07, 0.11

Source: Elaborated by the author.

4.2 Numerical Acquisition Data System

Before explore the experimental data with the Cessna 182 scaled aircraft, a simplified method was adopted to certify that the Neuro-Fuzzy is a good methodology to create an aerody-

namic model for aircrafts. The software used to acquire the numerical data is known as XPLANE, and it is a commercial flight simulator certified by the FAA.

In the software data base, it has a certain number of created commercial aircraft, as Boeing 737 and Cessna 172, which is very similar with Cessna 182, but with a substantially difference, only in pilots view, between both aircraft, the engine power.

However, the Cessna 182 was designed in the XPLANE flight simulator with the same dimensions of the scaled aircraft, however, with the parameters in the British unit system. The flight conditions were very similar, with the same Reynolds number, also was chosen the same weather conditions (clean with none or a few wind). The numerical data were acquired during the simulation of the aircraft flight. The Fig. 22 shows the XPLANE flight simulation for the Cessna 182 air model. The data showed on the left top window, is the telemetry for the aircraft.

Figure 22 – Cessna 182 air model flight on XPLANE.

Source: Elaborated by the author.

The flight scenario chosen was a calm atmosphere and clear weather, with few or none perturbation. The flight passed by some maneuvers and abrupt flight control deflections, based on the procedure presented by Brandon and Morelli (2012), justifying the moments oscillations during the training set that Chapter 5 will show.

4.3 Experimental Acquisition Data System

The acquisition data system used in this master thesis was a Pixhawk-PX4, which is an independent open-hardware low-cost developed by academic communities. To analyses the data acquired, it was used an open source software known as Mission Planner, which can communicate with the data acquisition board to help on data inspection and to create a access table for Matlab®.

Figure 23 – Pixhawk 3DR.

Source: px4.io (2019).

4.3.1 Pixhawk Configuration

The Pixhawk board can be configured through the software Mission Planner. In this case, the configuration followed the standard set up, with few changes, like an automatic triggering of data acquisition system as soon as the Pixhawk is powered up. The Fig. 24 shows the Mission Planner interface and the GPS image from the runaway flight road.

Figure 24 – Mission Planner interface.

Source: Elaborated by the author.

During the flight, the parameters shown in the left bottom part of Fig. 24, like yaw (*psi*), vertical velocity (W), altitude (H), among others, varies in real time, due the telemetry coupled to the Pixhawk. The Mission Planner also has an altimeter, shown in the left top from Fig. 24, which express the altitude of the aircraft and the velocity measured by the pitot tube.

4.4 Experimental Procedure

The Pixhawk was connected in the center of gravity of the airplane model, inside the cockpit, near the aerodynamic center of the wings, more precisely, and some extensions were

necessary to link the pitot tube and all servo motors, which are responsible to deflect the control surfaces, with the Pixhawk as shown in Fig. 25.

Figure 25 – Pixhawk servo connections.

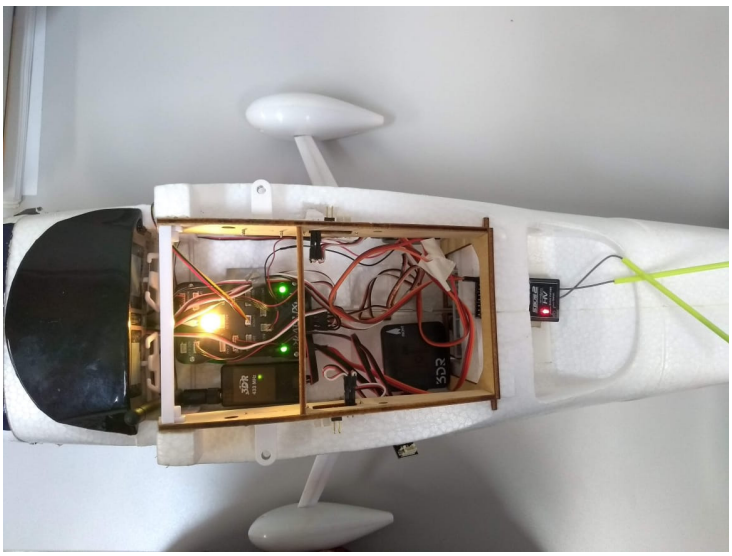

Source: Elaborated by the author.

After making all the connections, the airplane model was ready to flight, and the region chosen to flight was on the access road to UFU Campus Glória, few kilometers from the laboratory. The Fig. 26 shows the aircraft assembled and ready to fly on the flight runaway.

Figure 26 – Airplane model assembled and ready to fly.

Source: Elaborated by the author.

The flight had the total time duration of about 10 minutes and the same experimented the autonomous flight mode provided by Pixhawk, also the airplane started to follow the way points set in the Mission Planner before the flight. After reaching all the way points, the airplane

entered in the recovery control mode, where it begins to fly in circles whose center of the curve is the point of activation of the autonomous mode. The flight data were saved into a SD memory card inserted in the Pixhawk.

After the flight, the saved data was analyzed in the Mission Planner, and the region chosen to filter the data were around the autonomous flight mode, which the aircraft gained a great altitude to reach the way points, and then it started the circle movement, being a great region to train the longitudinal and the lateral-directional forces and moments.

4.4.1 Filter Implementation

The data acquired was very noisy, as a result of the aerodynamic vortexes provided by the propeller rotation. This problem was solved using a digital filter known as Savitzky-Golay, which has an implementation done in Matlab®. The Savitzky-Golay makes a polynomial interpolation between the desired amount of data points, smoothing the region of interest without distorting the signal tendency (PRESS *et al.*, 2007). The Fig. 27 shows the application of Savitzky-Golay filter in the Z axis accelerometer.

Figure 27 – Savitzky-Golay filter implementation.

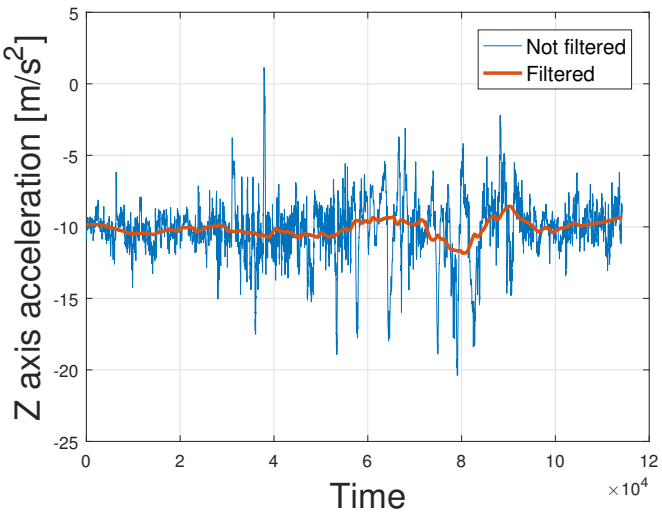

Source: Elaborated by the author.

After the filter implementation, the signals are ready to be trained as input and output variables of the Neuro-Fuzzy aerodynamic model.

4.4.2 Peason Correlation Coefficient

It is extremely necessary that the inputs have a similar curve with the output, or otherwise, the Neuro-Fuzzy will not be trained, because the technique imitates the input behavior to construct the fit curve for the output.

In this work, the methodology chosen to verify the correlation between the inputs with the output was the Pearson's correlation coefficient (PCC), described in Eq. 4.1. This correlation provides the relation between the input variable with the output, ensuring that the Neuro-fuzzy will be capable to be trained.

$$R_{xy} = \frac{\sum_{i=1}^{n}(x_i - \bar{x})(y_i - \bar{y})}{\sqrt{\sum_{i=1}^{n}(x_i - \bar{x})^2}\sqrt{\sum_{i=1}^{n}(y_i - \bar{y})^2}} \tag{4.1}$$

where, R_{xy} is the correlation between the input variable with the output variable, being x the input and y the output.

The correlation was applied only in the experimental data, because the numerical one had a clearly correlation, thus being unnecessary the use of the PCC. The Tab. 9 shows the correlation between the most influential inputs with the respective output.

Table 9 – Forces and Moments Pearson correlation coefficient with input variables.

	R_{xy}	Explanatory Variables
C_x	0.8902, -0.9299	α,U
C_y	0.9876, 0.9883	δ_a,δ_r
C_z	-0.8931, 0.9959	α,U
C_l	0.7616, 0.9598	β, R
C_m	0.7520, 0.7936	α,W
C_n	0.6266	$\dot{\beta}$

Source: Elaborated by the author.

The Tab. 9 provides which input variables, from Tab. 7, had more similarity with the forces and moments coefficients applied in the center of gravity of the aircraft.

4.5 Chapter Expectation

With all this process described, the data are ready to be trained. Thus, in the next two chapters, all the training and validation graphs will be presented, as well as the input variable influence into the output variable through a graph, for numerical and experimental data, respectively.

CHAPTER

5

NUMERICAL RESULTS

This chapter presents the aerodynamic modeling for Cessna 182 scaled with aid of the flight simulator known as XPLANE. The forces and moments will be separated into two main axis, the longitudinal axis and the lateral-directional axis to facilitate the analysis. In the following chapter, the experimental results, will be analyzed and, in the last chapter, both will be compared with to evaluate the accuracy from experimental data collected by the Pixhawk-PX4.

The XPLANE works with the forces in the wind axis as output, fact that implies the application of the rotation matrix. from Eq. 3.30, to set the lift, drag and side force to the body XYZ axis.

5.1 Longitudinal

In this subsection, will be presented the training and validation graphs for the forces in X and Z directions, therefore the moment around the Y axis. All the content of this subsection were acquired with the aid of the XPLANE flight simulator.

5.1.1 Force X

Applying the rotation matrix from Eq. 3.30, the force in the X axis could be written as:

$$F_X = -Dcos(\alpha)cos(\beta) - S_f cos(\alpha)sin(\beta) + Lsin(\beta) \tag{5.1}$$

where D is the drag force, S_f is the side force, L is the lift force, α is the angle-of-attack and β is the sideslip angle.

After obtain the F_x with the help of the rotation matrix, the coefficient (C_X) is obtained through the Eq. 5.2.

$$C_x = F_X/\hat{q}S \tag{5.2}$$

Then, the training region was selected, and it was performed using the angle of attack (α) and the elevator deflection (δ_e) as input variables. The Fig. 28 shows the behavior of the input variables and the output variable.

Figure 28 – Numerical correlation between the inputs with the output.

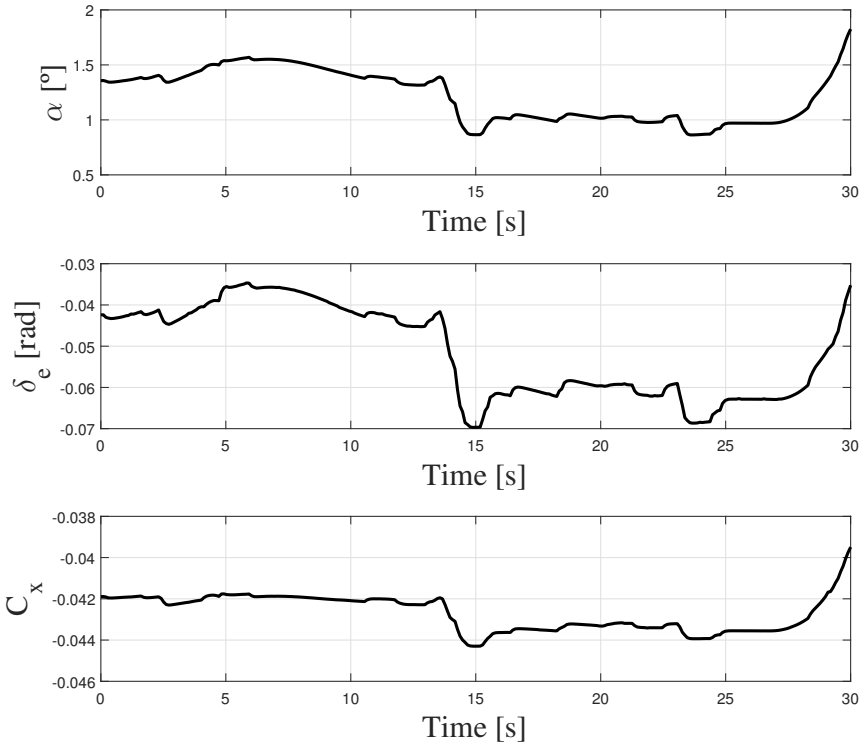

Source: Elaborated by the author.

After selected the training variables, the optimization was performed, using three membership functions for the input variables, defined as low, medium and high associated with five output zero order polynomial equations, that is, five constants, according with had been presented in Chapter 3 with the Takagi-Sugeno inference method. The training graph is presented in Fig. 29.

After the training, the means and standard deviations from the Gaussian's membership functions were obtained. It was used three membership functions for each input variable, to correlate with the output variables. The Tab. 10 shows the means and standard deviations for the input variables, while Tab. 11 shows the output coefficients.

To validate the training, a portion of the flight data that follows the training region was selected, as Fig. 30 shows.

Figure 29 – Numerical X force coefficient training graph.

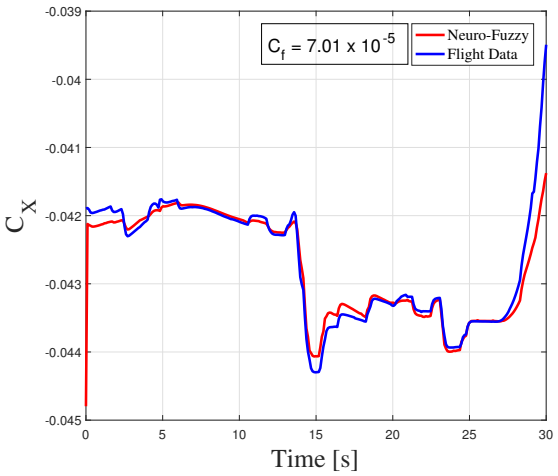

Source: Elaborated by the author.

Table 10 – Input means and standard deviations values from the Gaussian's membership functions for C_x training.

	Mean	Std
α	1.9416, 2.0647, 3.9132	1.8871, 2.3596, 0.2997
δ_e	-0.1000, -0.0026, 0.0500	0.0279, 0.0076, 0.0074

Source: Elaborated by the author.

Table 11 – Output zero order polynomial values.

	Coefficient
C_X	-0.0414, -0.0480, -0.0395, -0.4400, -0.3486

Source: Elaborated by the author.

Figure 30 – Numerical X force coefficient validation graphs.

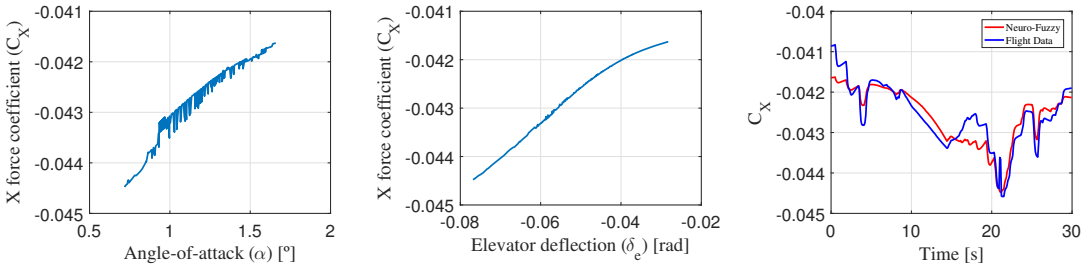

(a) $C_X x \alpha$ curve (b) $C_X x \delta_e$ curve (c) C_X validation.

Source: Elaborated by the author.

5.1.2 Force Z

Applying the same knowledge from X force coefficient, it is necessary to apply the rotation matrix presented in Eq. 3.30 to obtain the F_Z. Therefore, the F_Z can be written as:

$$F_Z = -Dsin(\alpha)cos(\beta) - S_f sin(\alpha)sin(\beta) - Lcos(\alpha) \tag{5.3}$$

After, the C_Z coefficient can be written as:

$$C_Z = F_Z/\overline{q}S \tag{5.4}$$

where $\overline{q}$ is the dynamic pressure and S is the wing reference area.

The training graph can be observed in Fig. 32 and the correlation between the inputs with the C_Z coefficient can be observed in Fig. 31.

Figure 31 – Numerical correlation between inputs with the output.

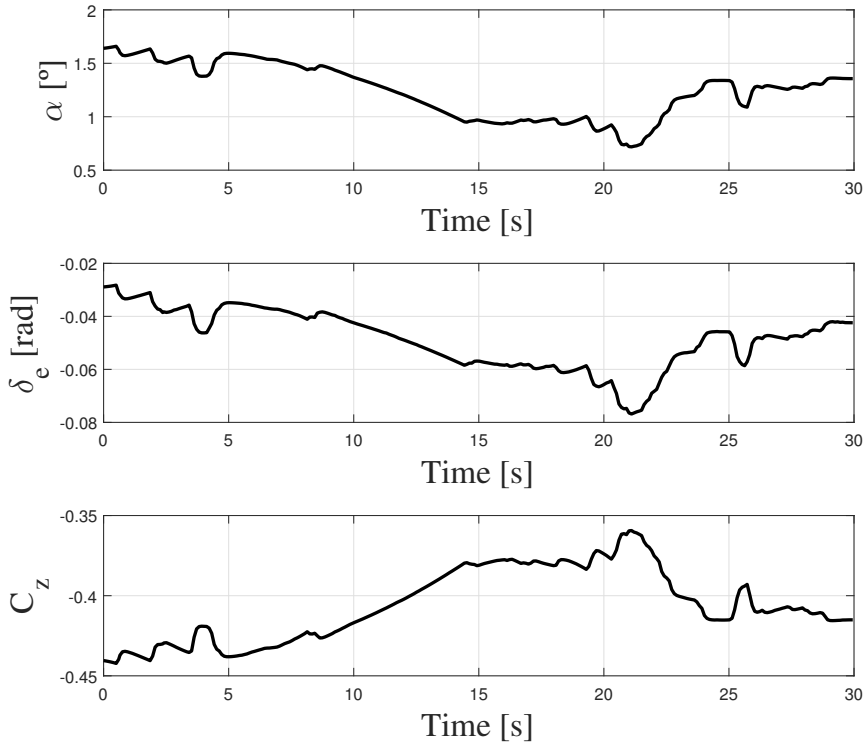

Source: Elaborated by the author.

After the training, the means and standard deviations were acquired to correlate the inputs with the output, which are the same inputs from X force coefficient, angle-of-attack (α) and elevator deflection (δ_e).

Tab. 12 shows the means and standard deviations for the input variables, while Tab. 13 shows the output coefficients.

To validate the training process, a portion of the flight data that follows the training region was selected, as Fig. 33 shows:

5.1.3 Moment M

The XPLANE flight simulator gives the moments value as output data using Eq. 3.40. Like the forces in longitudinal reference axis, the moment requires two input variables with the

Figure 32 – Numerical Z force coefficient training graph.

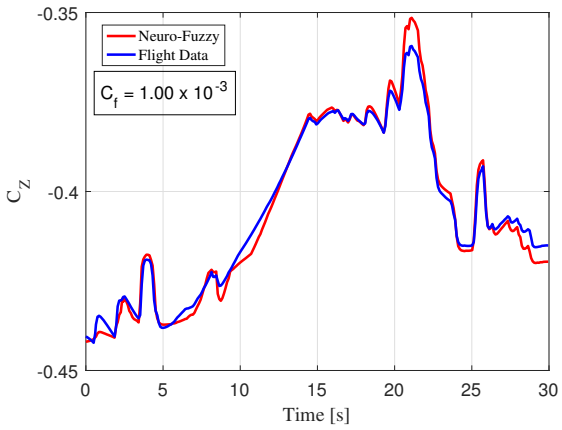

Source: Elaborated by the author.

Table 12 – Input means and standard deviations values from the Gaussian's membership functions for C_z training.

	Mean	Std
α	0.4175, 0.6165, 1.2004	0.3376, 0.4973, 0.4470
δ_e	-0.0600, -0.0611, -0.0600	0.0116, 0.0159, 0.0155

Source: Elaborated by the author.

Table 13 – Output zero order polynomial values.

	Coefficient
C_z	-0.6000, -0.4280, -0.3224, -0.2041, -0.1945

Source: Elaborated by the author.

Figure 33 – Numerical X force coefficient validation graphs.

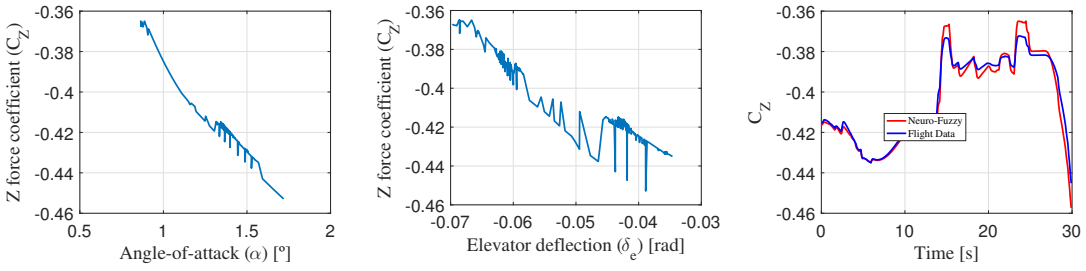

(a) $C_Z x \alpha$ curve (b) $C_Z x \delta_e$ curve (c) C_Z validation.

Source: Elaborated by the author.

highest correlation between all other variables prescribed by Roskam (1998) in Tab. 7, which are, in this case, the angle-of-attack rate ($\dot{\alpha}$) and the elevator deflection rate ($\dot{\delta}_e$).

In the same way, the training graph can be observed in Fig. 35 and the correlation between the inputs with the C_m coefficient can be observed in Fig. 34.

The differential evolution could predict the Gaussian parameters for input variables, in

Figure 34 – Numerical correlation between inputs with the output.

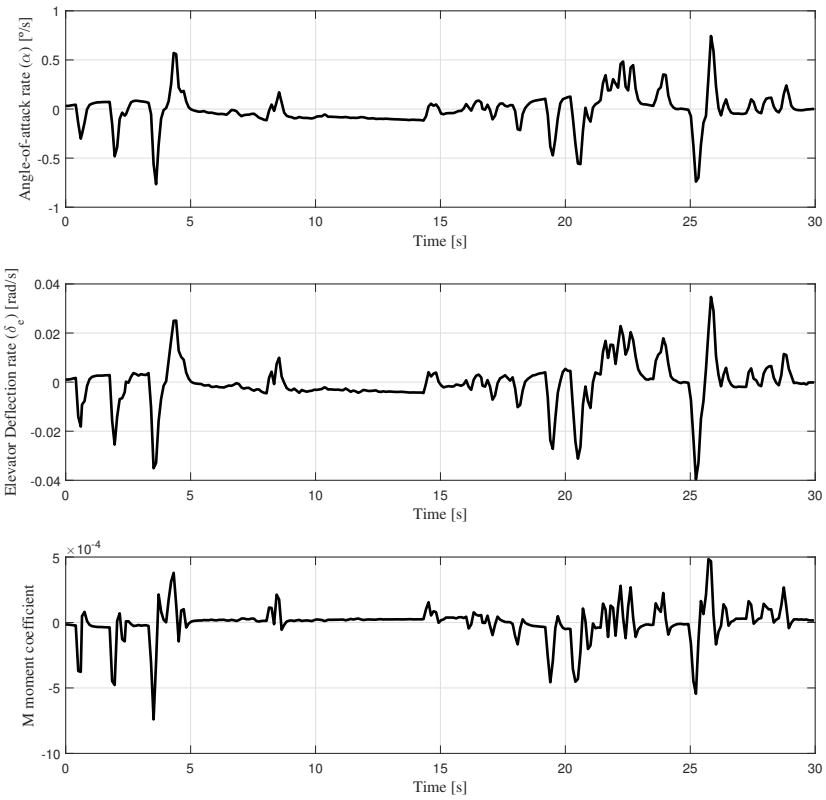

Source: Elaborated by the author.

Figure 35 – Numerical M moment coefficient training graph.

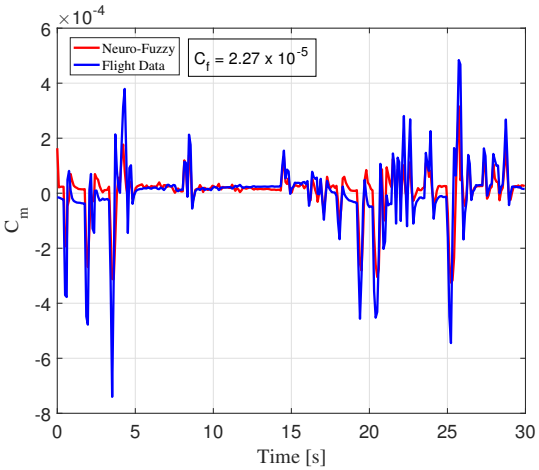

Source: Elaborated by the author.

addition, predicted the output coefficients as well.

The validation adopted the same portion of flight from the past models, and the graph is presented in Fig. 36.

Table 14 – Input means and standard deviations values from the Gaussian's membership functions for C_m training.

	Mean	Std
$\dot{\alpha}$	-1.0000, 0.5000, 0.6955	0, 0.1892, 0.4415
$\dot{\delta}_e$	-0.0500, 0.0033, 0.0208	0.0233, 0.0028, 0.0385

Source: Elaborated by the author.

Table 15 – Output zero order polynomial values.

	Coefficient
C_m	-0.0414, -0.0480, -0.0395, -0.4400, -0.3486

Source: Elaborated by the author.

Figure 36 – Numerical M moment coefficient validation graphs.

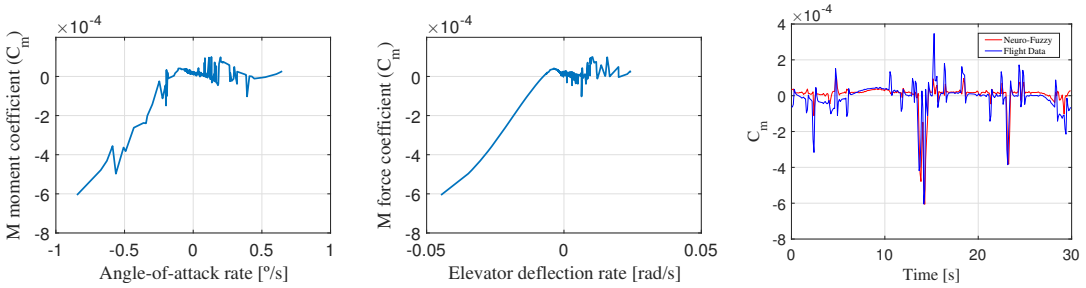

(a) $C_m x \alpha$ curve (b) $C_m x \delta_e$ curve (c) C_m validation.

Source: Elaborated by the author.

5.2 Lateral-Directional

In this reference axis, the most influential variables are defined in Tab. 7, and two of them were selected to train the force and moments, by the fact that two variables were chosen in the experimental models.

5.2.1 Force Y

The force in Y body axis could be written as:

$$F_y = -Dsin(\beta) + Scos(\beta) \tag{5.5}$$

Therefore, the Y force coefficient (C_Y) is defined as:

$$C_Y = F_Y / \bar{q}S \tag{5.6}$$

In the same way, the training graph can be observed in Fig. 38 and the correlation between the inputs with the C_Y coefficient can be observed in Fig. 37. Additionally, the Lateral-Directional has different influential variables, and for Cessna 182 the most influential variables for force Y are: sideslip angle (β) and rudder deflection (δ_r).

Figure 37 – Numerical correlation between inputs with the output.

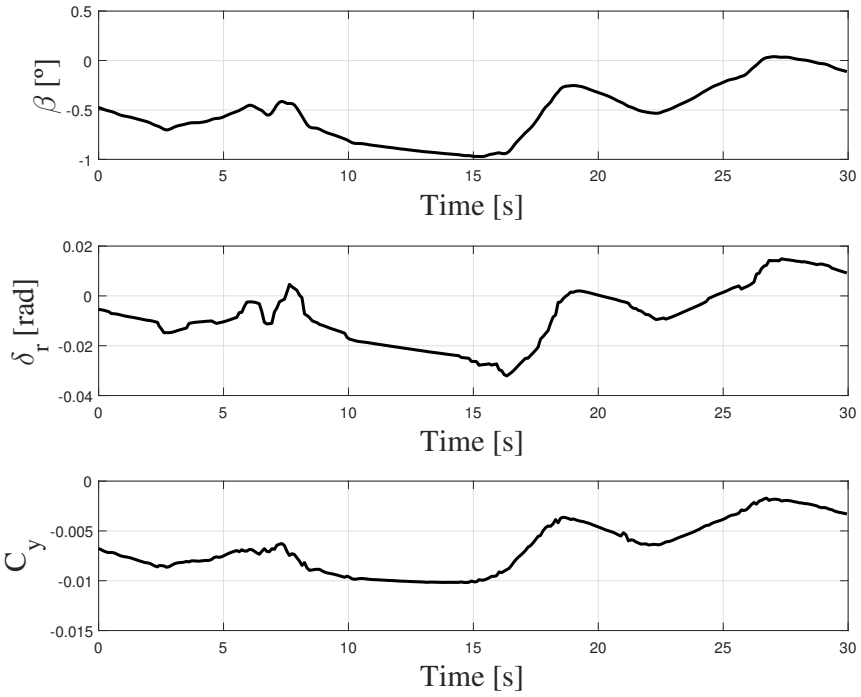

Source: Elaborated by the author.

Figure 38 – Numerical Y force coefficient training graph.

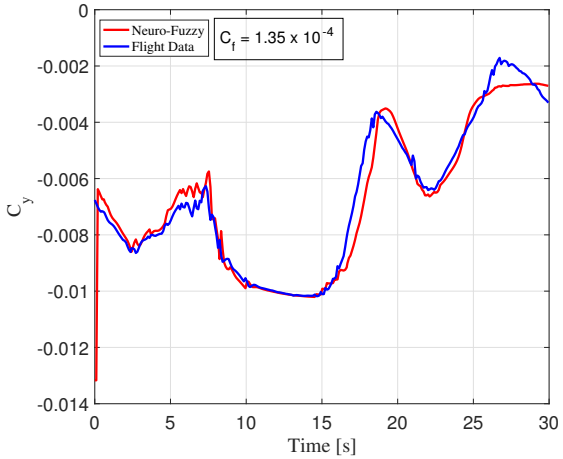

Source: Elaborated by the author.

The differential evolution could predict the Gaussian parameters for input variables, in addition, predicted the output coefficients as well.

To validate the training process, a portion of the flight data that follows the training region was selected, as Fig. 39 shows:

Table 16 – Input means and standard deviations values from the Gaussian's membership functions for C_Y training.

	Mean	Std
β	-0.6968, -0.3502, -0.1686	0.2984, 0.3000, 0.3000
δ_r	-0.0405, -0.0300, 0.0497	0.0081, 0.0206, 0.0055

Source: Elaborated by the author.

Table 17 – Output zero order polynomial values.

	Coefficient
C_Y	-0.0125, -0.0080, -0.0064, -0.0020, -0.0002

Source: Elaborated by the author.

Figure 39 – Numerical Y force coefficient validation graphs.

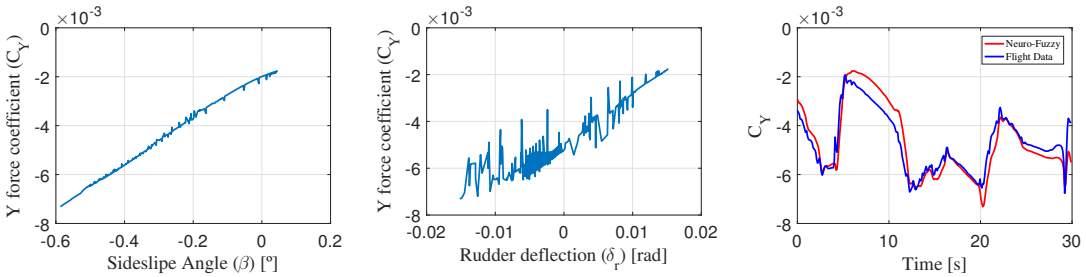

(a) $C_Y x \beta$ curve (b) $C_Y x \delta_r$ curve (c) C_Y validation.

Source: Elaborated by the author.

5.2.2 Moment L

Applying the same reason of Force Y, the training graph for the moment L can be observed in Fig. 38 and the correlation between the inputs with the C_l coefficient can be observed in Fig. 40. Additionally, the Lateral-Directional has different influential variables, and for Cessna 182 the most influential variables for moment L are: rudder deflection (δ_r) and aileron deflection (δ_a).

The differential evolution could predict the Gaussian parameters for input variables, in addition, predicted the output coefficients as well.

Table 18 – Input means and standard deviations values from the Gaussian's membership functions for C_l training.

	Mean	Std
δ_a	-0.1331, -0.1000, 0.0209	0.0454, 0.0643, 0.0723
δ_r	-0.0241, 0.0063, 0.0435	0.0289, 0.0050, 0.0476

Source: Elaborated by the author.

To validate the training process, a portion of the flight data that follows the training region was selected, as Fig. 42 shows:

Figure 40 – Numerical correlation between inputs with the output.

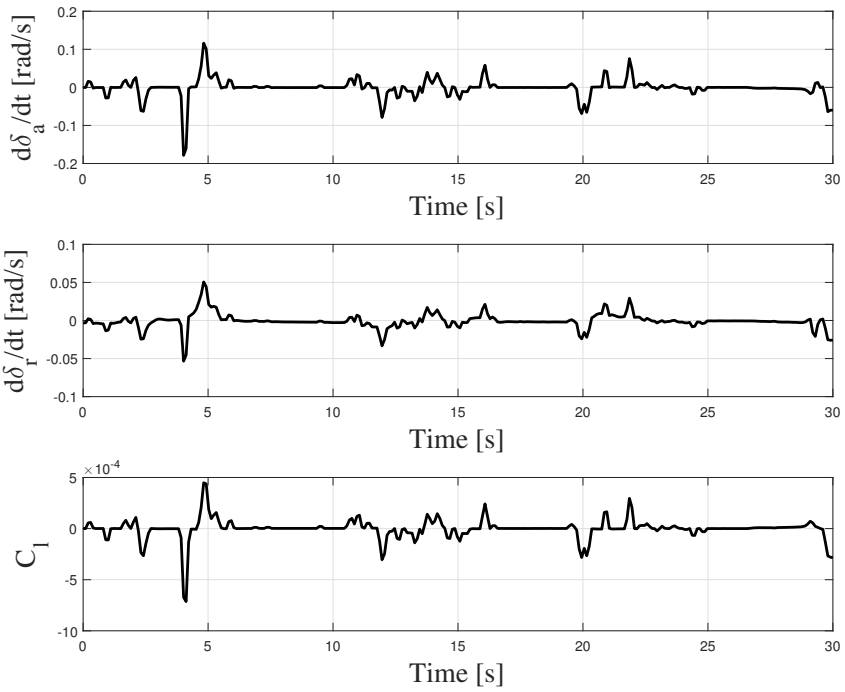

Source: Elaborated by the author.

Figure 41 – Numerical L moment coefficient training graph.

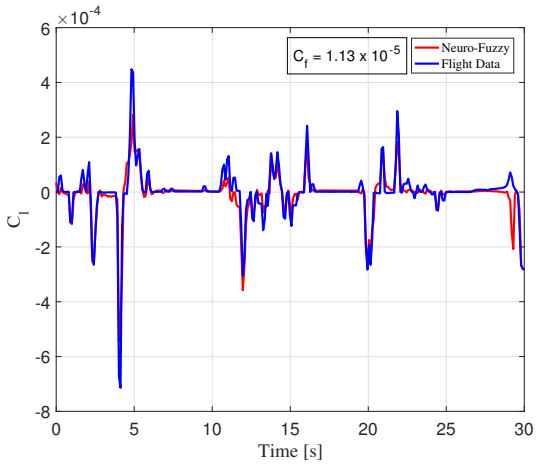

Source: Elaborated by the author.

Table 19 – Output zero order polynomial values.

	Coefficient
C_l	-0.0004, -0.0005, 0, -0.0001, 0.0005

Source: Elaborated by the author.

Figure 42 – Numerical L moment coefficient validation graphs.

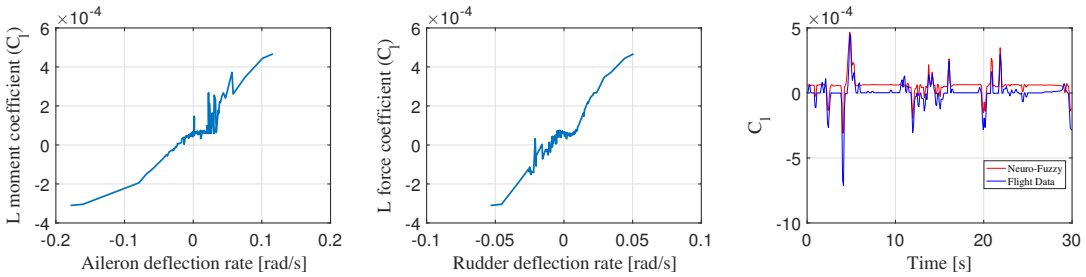

(a) $C_l x \delta_a$ curve (b) $C_l x \delta_r$ curve (c) C_l validation.

Source: Elaborated by the author.

5.2.3 Moment N

The moment N was the last model, ending the numerical modeling. It could be observed, that the moment N for the Cessna 182 air model does not have many influential variables. As well as the experimental data training for moment N, only one input variables has high correlation with the moment, and this variables for the numerical data is the aileron deflection (δ_a).

The Fig. 43 shows the correlation between the input and output graphs. Also, the approximation built by the Neuro-Fuzzy with the training numerical data can be observed in Fig. 44.

Figure 43 – Numerical correlation between inputs with the output.

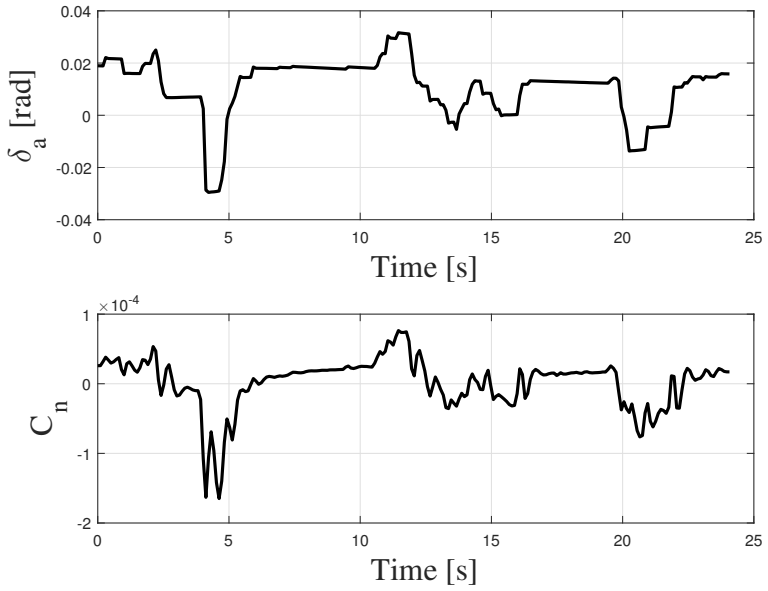

Source: Elaborated by the author.

The parameters predicted by the differential evolution can be seen in Tab 20 and Tab. 21.

To validate the training process, a portion of the flight data that follows the training

Figure 44 – Numerical N moment coefficient training graph.

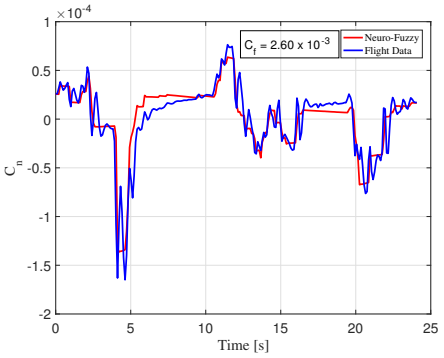

Source: Elaborated by the author.

Table 20 – Input means and standard deviations values from the Gaussian's membership functions for C_n training.

	Mean	Std
δ_a	-0.0300, 0.0050, 0.0277	0.0065, 0.0187, 0.0200

Source: Elaborated by the author.

Table 21 – Output zero order polynomial values.

	Coefficient
C_n	-0.0001, -0.0001, 0.0001

Source: Elaborated by the author.

region was selected, as Fig. 45 shows:

Figure 45 – Numerical N moment coefficient validation graphs.

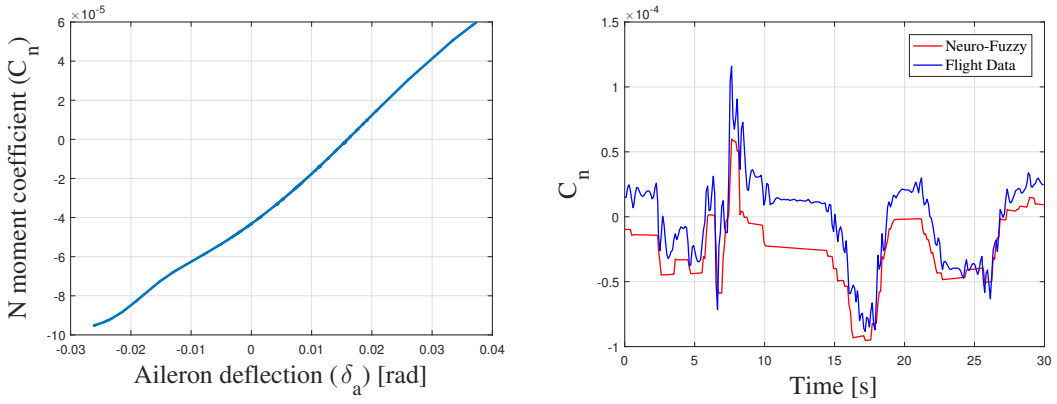

(a) $C_n x \delta_a$ curve (b) C_n validation.

Source: Elaborated by the author.

5.3 Chapter Expectation

This section exposed every training, validation and correlation graphs for numerical data. The next chapter will be present the same proceeding, therefore for the experimental results. The conclusion will be presented in this master thesis last chapter.

CHAPTER

6

EXPERIMENTAL RESULTS

This chapter will present the aerodynamic modeling for Cessna 182 scaled with the aid of Pixhawk-PX4 data acquisition system. The forces and moments will be separated into two main axis, like the past chapter, the longitudinal axis and the lateral-directional axis to facilitate the analysis. In the following chapter, the results from experimental will be exposed and, in the next chapter, compared with the numerical results to evaluate the accuracy from experimental data collected by the Pixhawk-PX4.

According to Fossen (2011), the acceleration in the three body axis, given by the accelerometers, can be written as:

$$a_{x_{CG}} = \frac{X}{m} = \dot{U} + QW - RV + gsin(\theta) \tag{6.1}$$

$$a_{y_{CG}} = \frac{Y}{m} = \dot{V} + UR - WP - gcos(\theta)sin(\phi) \tag{6.2}$$

$$a_{z_{CG}} = \frac{Z}{m} = \dot{W} + VP - QU - gcos(\theta)cos(\phi) \tag{6.3}$$

In addition, according to Chang (2013), the moments coefficients can be calculated through the gyroscope data (P, Q and R):

$$C_l \overline{q} Sb = I_{xx}\dot{P} - I_{xz}\dot{R} + QR(I_{zz} - I_{yy}) - I_{xz}PQ \tag{6.4}$$

$$C_m \overline{q} S\overline{c} = I_{yy}\dot{Q} + RP(I_{xx} - I_{zz}) + I_{xz}(P^2 - R^2) - T_m \tag{6.5}$$

$$C_n \overline{q} Sb = -I_{xz}\dot{P} + I_{zz}\dot{R} + PQ(I_{yy} - I_{xx}) + I_{xz}QR \tag{6.6}$$

6.1 Longitudinal

This section will present the results from the aerodynamic model created for the analyzed aircraft in the longitudinal axis. The accelerometer signal multiplied by the aircraft mass, provides the aerodynamic forces.

6.1.1 Force X

The acceleration on the X axis, from the Inertial Measurement Unit (IMU) directly connected to the Pixhawk, multiplied by the mass of the aircraft is equivalent to the aerodynamic force on the X axis, as Eq. 6.1 shows. Thus, the force on X axis is given by:

$$F_x = m.a_{x_{CG}} \tag{6.7}$$

According to Eq. 3.13, the X force coefficient is:

$$C_x = F_x/\overline{q}S \tag{6.8}$$

The acquisition data was carefully analyzed to decide the most appropriated flight situation to analyze the longitudinal forces and moments. The portion of the flight selected to do the Neuro-Fuzzy model training was in the region of the highest altitude variation found in the telemetry log review.

With the Pearson's correlation equation, it was possible to find the most influential control variables for the X force in the Cessna 182 scaled air model. All control variables proposed by Roskam (1998) cited in Tab. 7 were took in consideration. The Tab. 9 shows the most influential input parameter for the X force coefficient (C_x). The train time for all forces and coefficient were about 500 seconds.

In Fig. 46 is possible to observe the correlation between angle-of-attack and u-velocity (both inputs) with the output C_X, being directly and reverse correlation, respectively.

It is notable that the X force coefficient increases proportionately with the angle-of-attack, which means that the increment of the angle-of-attack increases the induced drag (C_{D_i}), reducing the velocity in X direction (u-velocity). Therefore, the electric motor thrust must increase to compensate the velocity reduction, increasing the X force.

The Fig. 47 shows the Neuro-Fuzzy fit approximation graph with the flight data graph, it is possible to observe that the training process resulted in a great polynomial approximation.

The trained mean, standard deviations and constants for Takagi-Sugeno fuzzy inference method are shown in Tab 22 and 23:

After obtain the Gaussian coefficients and the constant from the first degree polynomial, values for C_x were obtained from α and u-velocity in a different part of the flight, more precisely, in the next 30 seconds of flight. The relation between X force coefficient and the input variables

Figure 46 – Inputs and output correlation graphs for training.

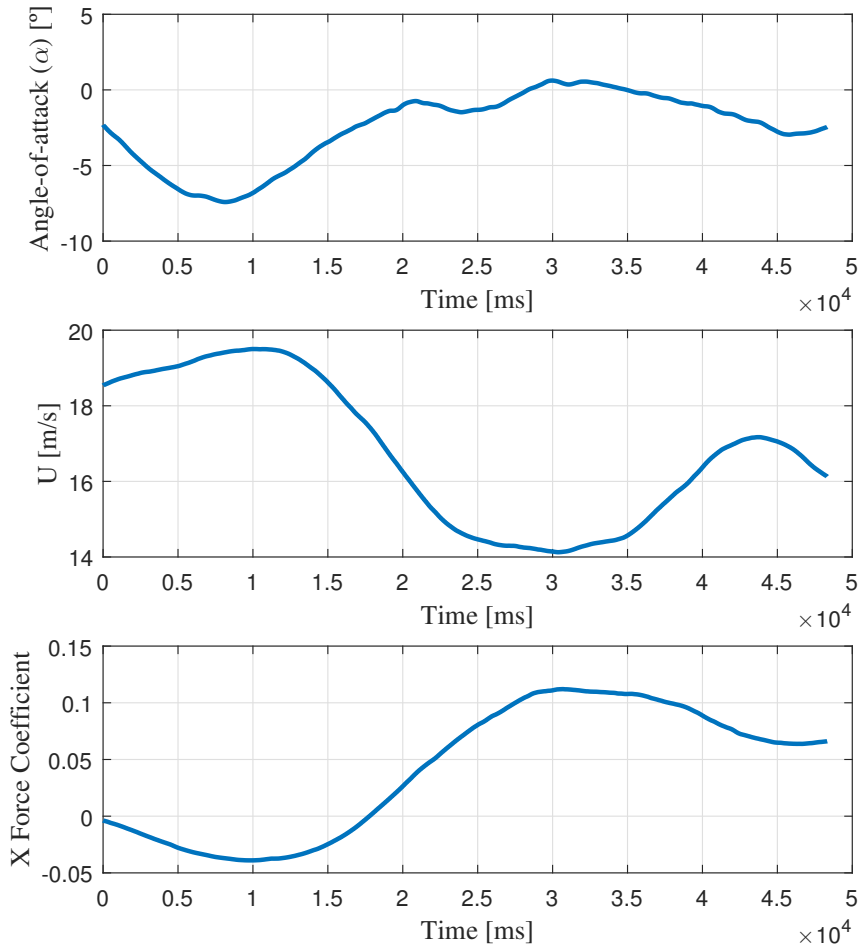

Source: Elaborated by the author.

Table 22 – Input means and standard deviations values from the Gaussian's membership functions for C_x training.

	Mean	Std
α	-5.9864, -2.3178, 3.0000	0.8877, 0.9066, 2.5667
u-velocity	11.3172, 12.9712, 18.4247	2.5000, 2.3324, 0.4862

Source: Elaborated by the author.

Table 23 – Output zero order polynomial values for C_x.

	Coefficient
C_x	-0.0378, 0.0015, 0.0353, 0.0600, 0.1504

Source: Elaborated by the author.

(α and u-velocity) were analyzed, the equation for C_{x_α} and C_{x_U}, were a first or second degree polynomial, as Fig. 48 shows.

Figure 47 – Experimental X force coefficient training graph.

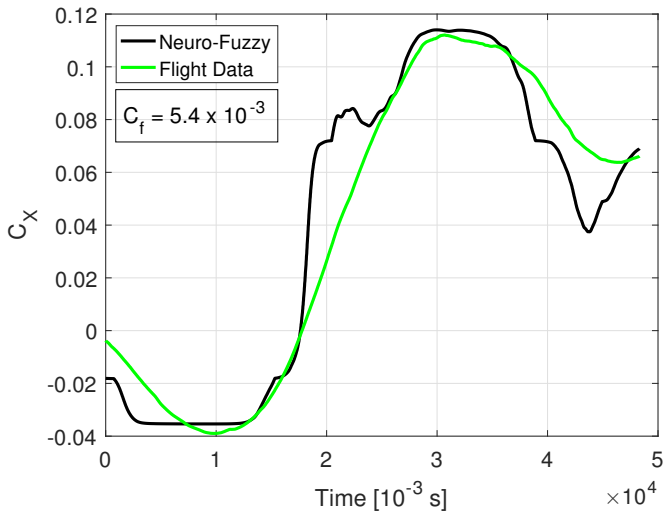

Source: Elaborated by the author.

Figure 48 – Experimental X force coefficient validation graphs.

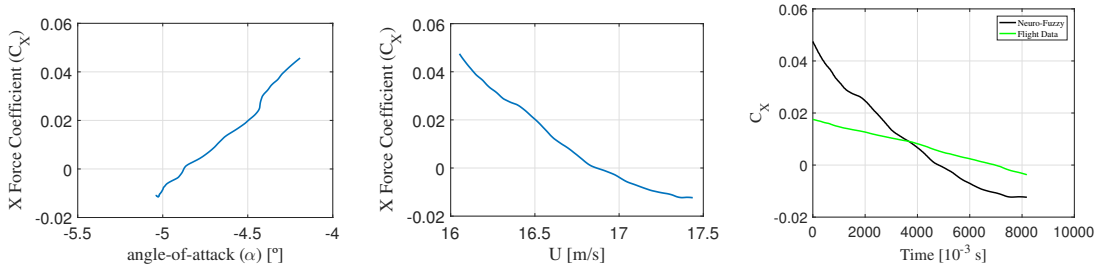

(a) $C_x x\alpha$ curve. (b) $C_x xu$ curve. (c) C_X validation.

Source: Elaborated by the author.

6.1.2 Force Z

According to Fossen (2011), F_z is the acceleration acquired by the accelerometer coupled in the IMU from Pixhawk multiplied by the aircraft mass. The equation below shows the Z force equation for the air model.

$$F_z = m.a_{z_{CG}} \tag{6.9}$$

In this case, m is the aircraft mass and is equivalent a 1.5 kg, as shown in Tab. 8, with all embedded electronics, and $a_{z_{CG}}$ is the accelerometer measurement for the Z direction acceleration. The Z force coefficient can be calculated with Eq. 3.16.

In Fig. 49 is possible to observe the correlation between angle-of-attack and u-velocity (both inputs) with the output C_z, being inverse and directly correlation, respectively. Again, the angle-of-attack increment decreases the Z force coefficient, because the Z body axis is pointed to the ground.

The Fig. 50 shows the Neuro-Fuzzy fit approximation graph with the flight data graph, it

Figure 49 – Experimental inputs and output correlation graphs for training.

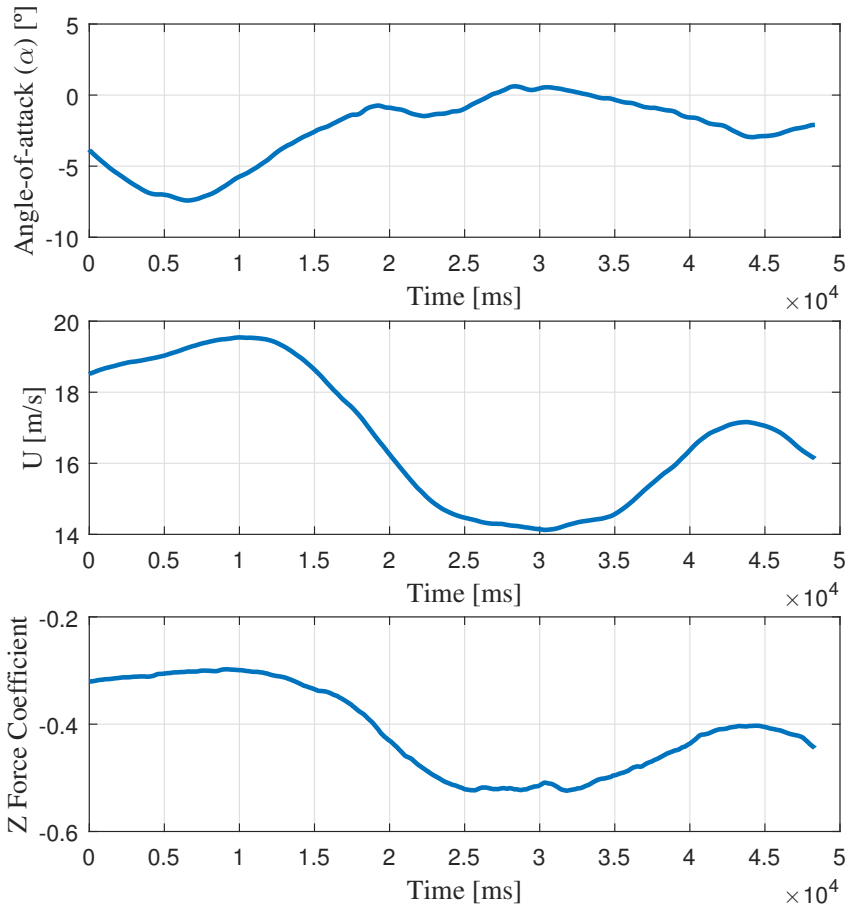

Source: Elaborated by the author.

is possible to observe that the training process resulted in a great polynomial approximation.

The trained mean, standard deviations and constants for Takagi-Sugeno fuzzy inference method are shown in Tab 24 and 25:

Table 24 – Input means and standard deviations values from the Gaussian's membership functions for C_z training..

	Mean	Std
α	-5.03, -1.39, -0.36	1.33, 2.66, 1.35
u-velocity	15.00 15.50 20.00	4, 0.1, 2.46

Source: Elaborated by the author.

Table 25 – Output zero order polynomial values.

	Coefficient
C_z	-0.38, -0.35, -0.18, -0.13, - 0.09

Source: Elaborated by the author.

Figure 50 – Experimental Z force training graph.

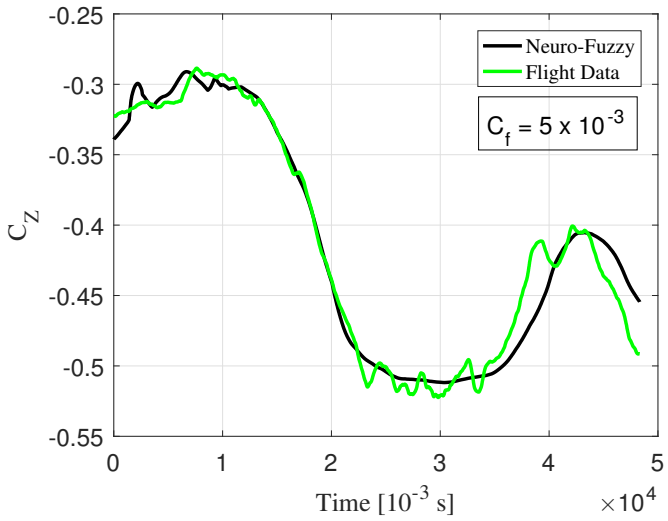

Source: Elaborated by the author.

In this case, the relation between Z force coefficient and the input variables (α and $u - velocity$) it was possible to obtain the equation for C_{z_α} and C_{z_u}, as shown in Fig. 51.

Figure 51 – Experimental Z force coefficient validation graphs

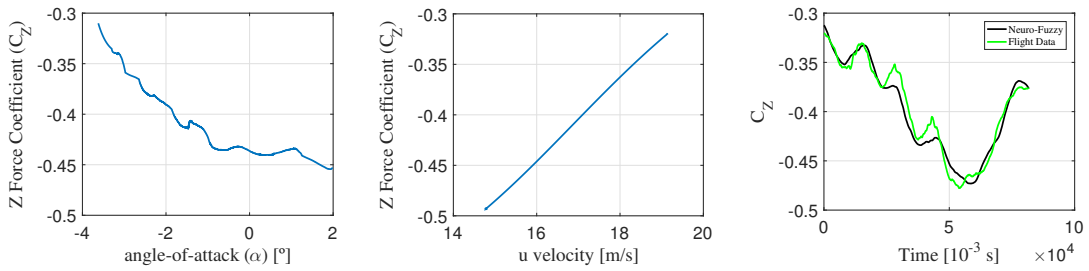

(a) $C_z x \alpha$ curve (b) $C_z xu$ curve (c) C_Z validation.

Source: Elaborated by the author.

6.1.3 Moment M

According to Chang (2013), the moment coefficient in the Y direction, can be calculated using Eq. 6.5, where $\overline{q}$ is the dynamic pressure, S is the wing area, b is the wing span, I_{xx}, I_{yy} and I_{zz} are the inertia moments, P is the roll rate, Q is the pitch rate, R is the yaw rate, I_{xz} is the inertia product and T_m is the torque, bot are negligible, because of the aircraft symmetry.

In Fig. 52 is possible to observe the correlation between angle-of-attack and w-velocity (both inputs) with the output C_m. The inputs has directly correlation with the output. The input variables were chosen according to Tab. 9 shown in the past chapter.

The curve fit for the M moment coefficient training is shown in Fig.53.

Figure 52 – Experimental inputs and output correlation graphs for M moment coefficient training.

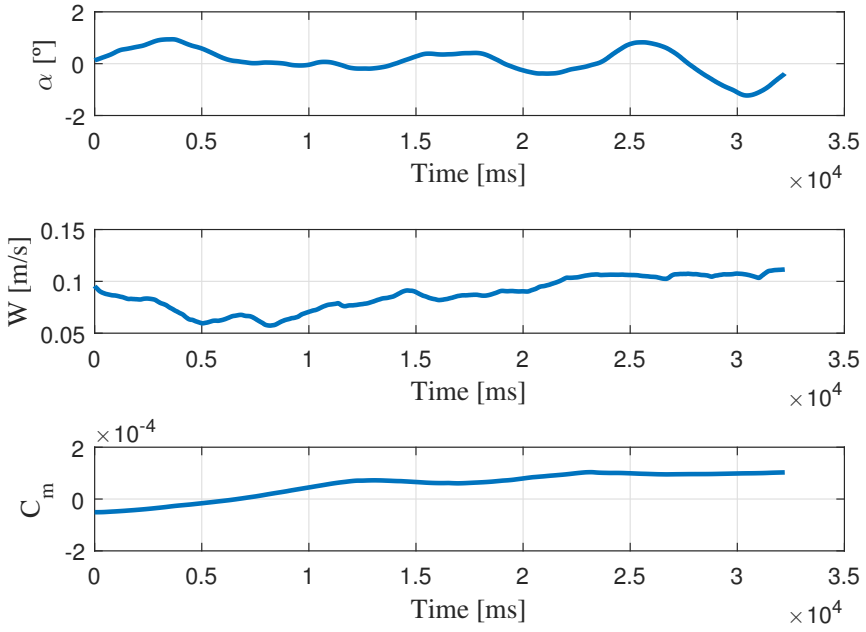

Source: Elaborated by the author.

Figure 53 – Experimental M moment coefficient training graph.

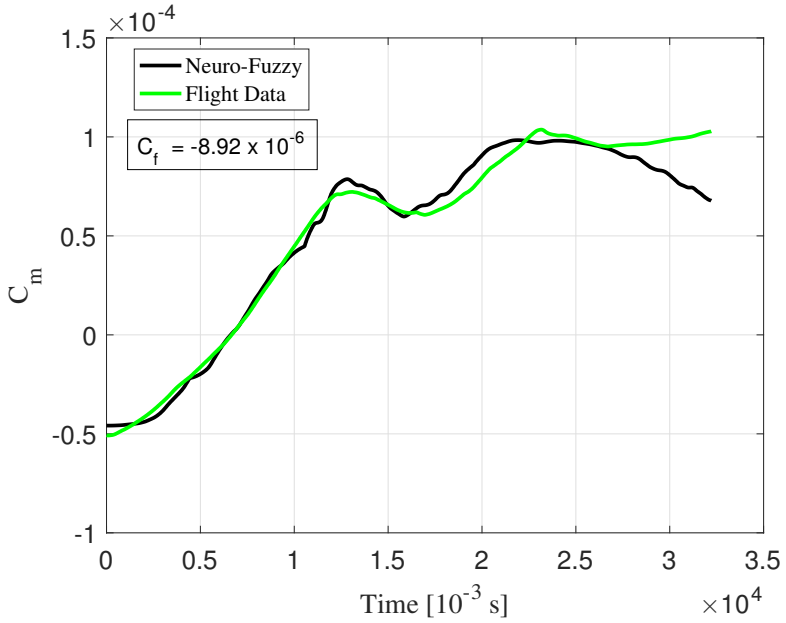

Source: Elaborated by the author.

After the training process, the coefficients from the input membership functions were acquired as shown in Tab. 26, also the coefficients for the constants zero degree polynomial values are shown in Tab. 27.

Table 26 – Input means and standard deviations values from the Gaussian's membership functions for C_m training..

	Mean	Std
α	-6.5726, -5.9804, -2.7310	1.0862, 1.1186, 1.1394
w-velocity	-1.3620, -1.1373, 0.0532	0.3478, 0.5080, 0.5453

Source: Elaborated by the author.

Table 27 – Output zero degree polynomial values.

	Coefficient
C_m	$-4.75x10^{-6}$, $2.09x10^{-6}$, $-1.91x10^{-6}$, $2.00x10^{-6}$, $10.0x10^{-6}$

Source: Elaborated by the author.

After the training process, the optimized fuzzy parameters were applied in the validation, using a different portion of the flight, as show in Fig. 54.

Figure 54 – Experimental M moment coefficient validation graphs

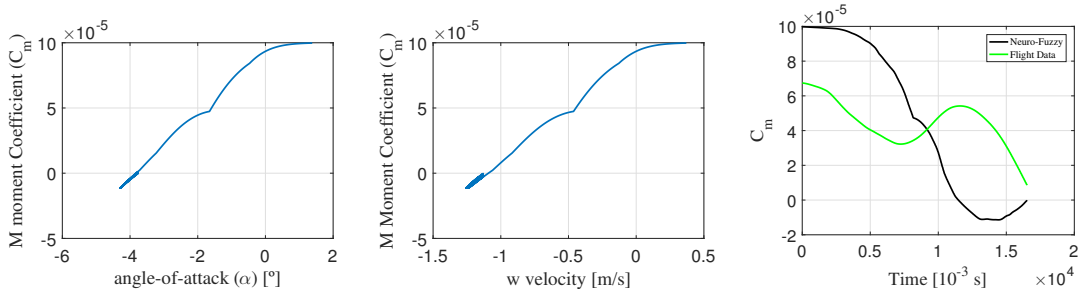

(a) $C_m x \alpha$ curve (b) $C_m xw$ curve (c) C_m validation.

Source: Elaborated by the author.

6.2 Lateral-Directional

This subsection will present the results from the aerodynamics model created for the analyzed aircraft on the lateral-directional axis. The Euler angles rate (roll, pitch and yaw) were take in considering to estimate the moments coefficients.

6.2.1 Force Y

Similar with the other forces in the longitudinal axis, the force in the Y axis is given as by the Eq. 3.21, in which F_y is the accelerometer signal in the Y axis ($a_{z_{CG}}$) multiplied by the aircraft mass (m).

The Fig. 55 shows the correlation between the inputs with the output, which are, according to Tab. 9, the aileron deflection (δ_a) and rudder deflection (δ_r).

Figure 55 – Experimental Y force coefficient correlation with inputs.

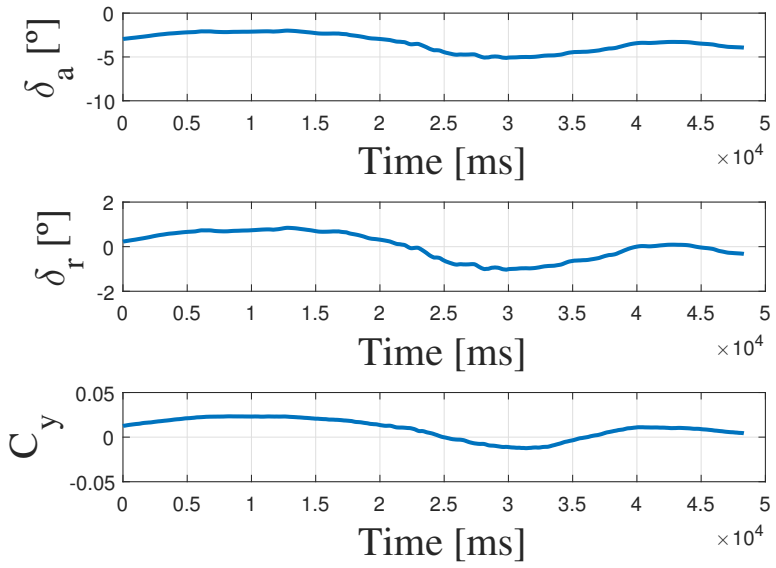

Source: Elaborated by the author.

Figure 56 – Experimental Y force coefficient training graph.

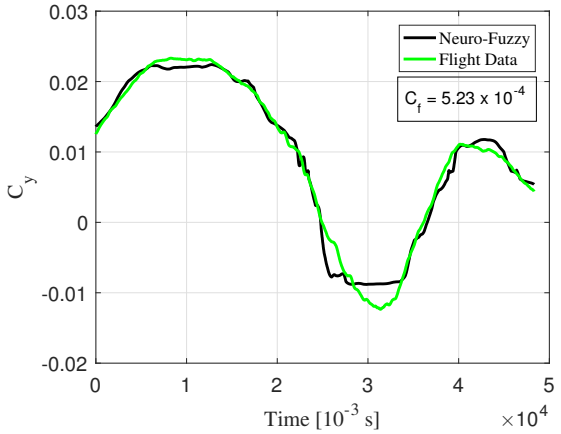

Source: Elaborated by the author.

The curve fit for the training set can be observed in Fig. 56.

The membership function coefficients and the output constant coefficient optimized are shown in Tab. 28 and Tab. 29.

Table 28 – Input means and standard deviations values from the Gaussian's membership functions for C_y training..

	Mean	Std
δ_a	-5.1344, -3.5950, -1.9844	0.8577, 0.5348, 0.8603
δ_r	-0.9994, -0.4618, 0.3457	0.3711, 0.4702, 0.4149

Source: Elaborated by the author.

Table 29 – Output zero order polynomial values.

	Coefficient
C_y	-0.0092, 0.0005, 0.0087, 0.0120, 0.0238

Source: Elaborated by the author.

To validate the the model created for Y force coefficient, a different portion of the flight was selected. The Fig. 57 shows the validation graphs and the behavior of C_Y with the aileron and rudder deflection.

Figure 57 – Y force coefficient validation graphs.

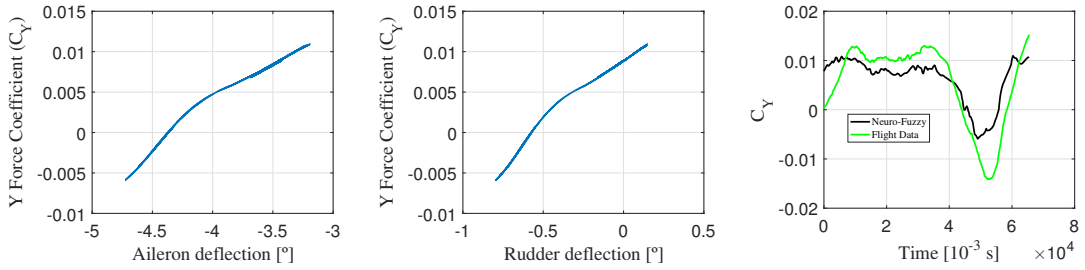

(a) $C_Y x \delta_a$ curve (b) $C_Y x \delta_r$ curve (c) C_Y validation.

Source: Elaborated by the author.

6.2.2 Moment L

Similar with the other moment in the longitudinal axis, the moment around the X axis is given as by the Eq. 3.20.

The Fig. 58 shows the correlation between the inputs with the output.

The curve fit for the training set can be observed in Fig. 59

The membership function coefficients and the output constant coefficient optimized are shown in Tab. 30 and in Tab. 31.

Table 30 – Input means and standard deviations values from the Gaussian's membership functions for C_l training..

	Mean	Std
β	-0.1687, -0.1007, -0.0440	0.0854, 0.0243, 0.0002
R	-1.8304, 0.3764, 2.9691	1.2969, 1.8350, 1.8990

Source: Elaborated by the author.

To validate the the model created for L moment coefficient, a different portion of the flight was selected. The Fig. 60 shows the validation graphs and the relation of C_l with the input variables.

Figure 58 – Experimental L moment coefficient correlation with inputs.

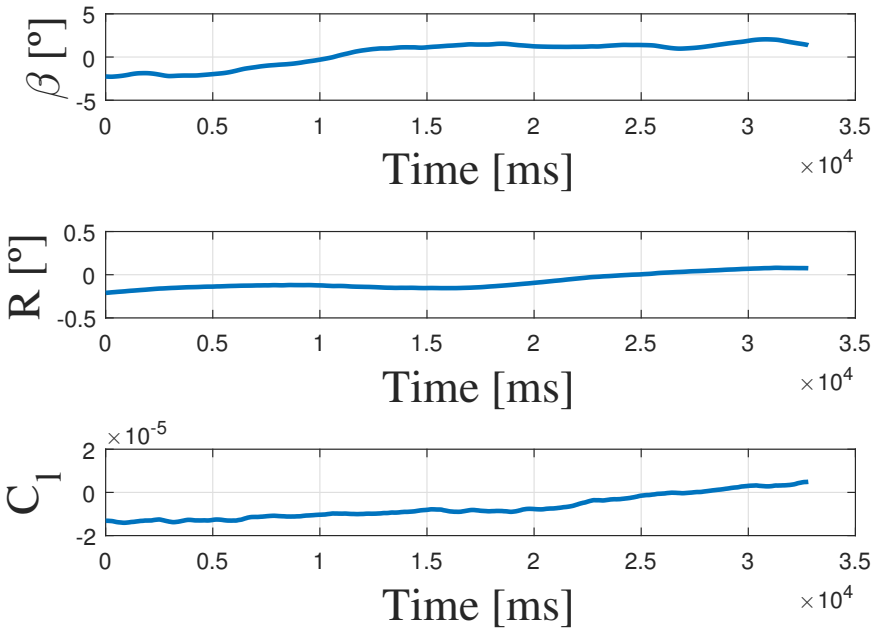

Source: Elaborated by the author.

Figure 59 – Experimental L moment coefficient training graph.

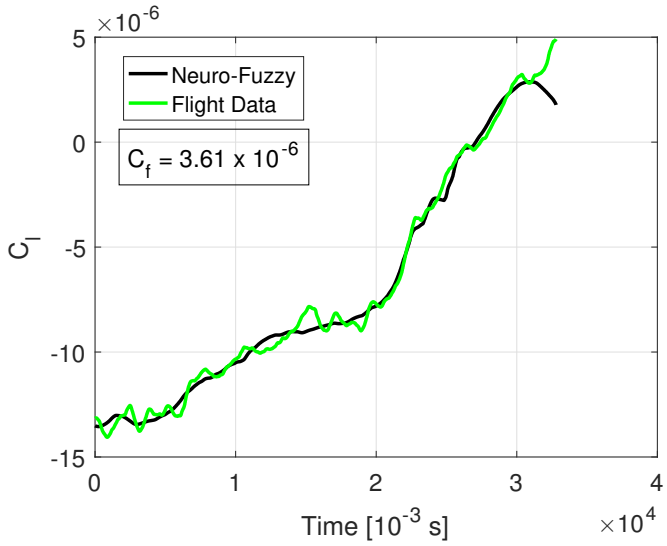

Source: Elaborated by the author.

Table 31 – Output zero order polynomial values.

	Coefficient
C_l	-0.000015, -0.000012, -0.000009, -0.000006, 0.000004

Source: Elaborated by the author.

Figure 60 – L moment coefficient validation graphs.

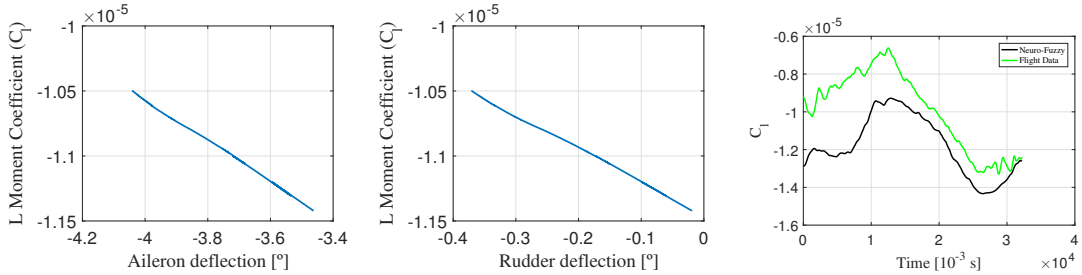

(a) $C_l x \delta_a$ curve (b) $C_l x \delta_r$ curve (c) C_l validation.

Source: Elaborated by the author.

6.2.3 Moment N

The moment around Z axis presented only one variable with a high correlation coefficient, as shown in Tab. 9. To estimate the N moment, the Eq. 3.22 was used. In the case of the moment N, only one variable has the PCC above 0.8, and it is the sideslip angle rate ($\dot{\beta}$).

The Fig. 61 shows the correlation between the input with the output.

Figure 61 – Experimental N moment coefficient correlation with input.

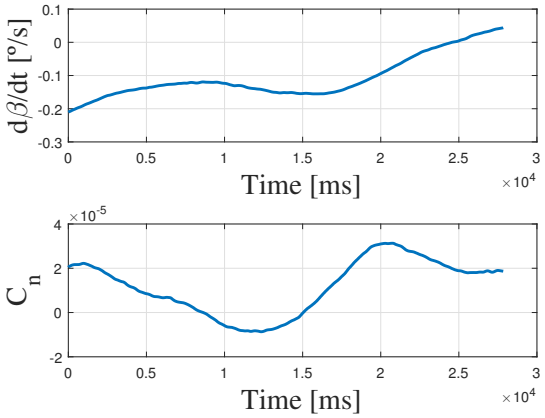

Source: Elaborated by the author.

The curve optimization for the training set, with aid of the differential evolution, can be observed in Fig. 62.

The membership function coefficients and the output constant coefficient optimized are shown in Tab. 32 and in Tab. 33.

To validate the the model created for L moment coefficient, a different portion of the flight was selected. The Fig. 63 shows the validation graphs and the relation of C_n with the input variables.

Figure 62 – Experimental N moment coefficient training graph.

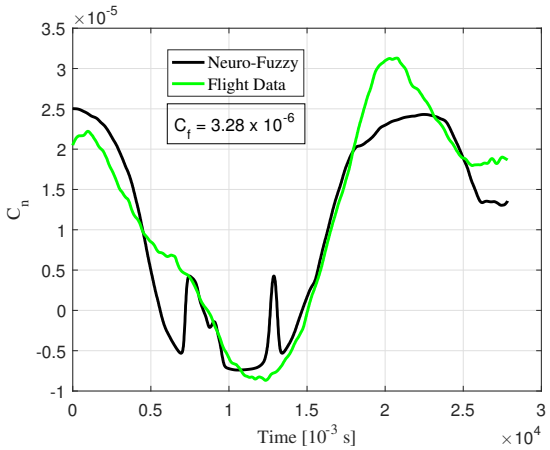

Source: Elaborated by the author.

Table 32 – Input means and standard deviations values from the Gaussian's membership functions for C_n training..

	Mean	Std
$\dot{\beta}$	-0.0500, 0.1562, 0.2052	0.0717, 0.0090, 0.0889

Source: Elaborated by the author.

Table 33 – Output zero order polynomial values.

	Coefficient
C_n	-0.0000075, 0.0000155, 0.0000253

Source: Elaborated by the author.

Figure 63 – N moment coefficient validation graphs.

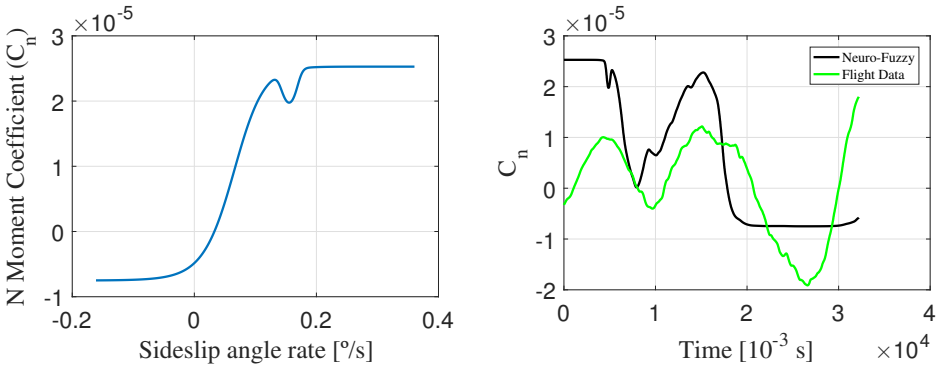

(a) $C_n x \dot{\beta}$ curve. (b) C_n validation graph.

Source: Elaborated by the author.

6.3 Chapter Expectation

The moment N validation graph showed, was purposeful to demonstrate the conclusion pointed by Brandon and Morelli (2012), which affirms that the Neuro-Fuzzy can not extrapolate

the training boundaries. In Fig. 63, the minimum moment N coefficient is almost $-2x10^{-5}$, being that in the training graph, presented in Fig. 62, the minimum moment N coefficient is $-0.75x10^{-5}$. To close this master thesis, the next chapter will present the conclusions and future works for the presented work.

CHAPTER

7

CONCLUSION AND FUTURE WORKS

The numerical and experimental results presented on chapter 5 and chapter 6, showed that the training process for most forces and moments were successfully done. Therefore the moments for experimental data did not presented a good validation, because the values of the moment coefficients are very low.

The validation results, sometimes, presented a inverse correlation between inputs with the output variable. In Fig. 54 it is evident that the input variables, angle-of-attack (α) and w velocity do not correlate with the C_m, but in the training flight interval used, they correlated very well. This incoherence can be due some perturbations during the flight interval or a misunderstand use of the filters, which can distort the real dynamics of the aircraft.

The acquisition board (Pixhawk-PX4) uses the GPS signal along with the velocity measured by the pitot tube to calculate the angle-of-attack, during the flight interval applied to validate the longitudinal forces model, a little interference could happened in the GPS data signal, because only the u velocity is compatible with the output force coefficient (C_X). However, is more obviously that the powertrain changed the aircraft characteristic, once this aerodynamic model did not evaluated the thrust curve for the electric motor used in Cessna 182 air model.

The numerical results are very closely, in scale, if compared with the experimental results, the main scale difference is presented on the moment graphs, which granted a difference in order of one or two decimal scale.

The experimental results showed that some stability derivatives are non-linear, like $C_{n_{\dot{\beta}}}$ and C_{z_α} expressed in Fig. 51 and Fig. 63, contradicting the approximations proceeded by numerical and theoretical modelling, which consider the stability derivatives as constant parameters. The results confirm that sometimes they are just a constant, otherwise, they assume an equation form.

At the end of the development of this work, from the analysis carried out and the results obtained, the following suggestions are proposed for its continuity:

- Apply the Neuro-Fuzzy technique on bigger air models, which has more expressive moments of inertia.
- Implement the *machine learning* technique on the Neuro-Fuzzy models, in order to extrapolate the training limits.
- Acquire richer data from the flight test, encompassing stall recovery, that one may model non-linear high order aerodynamic stability derivatives.

BIBLIOGRAPHY

Aeronef.net. **Cessna 182 the Skylane Aircraft Wallpaper 2321**. 2019. <https://www.aeronef.net/2012/02/cessna-182-skylane-aircraft-wallpaper.html>, Last accessed on 2019-05-23. Citation on page 64.

BRANDON, J. M.; MORELLI, E. A. Nonlinear aerodynamic modeling from flight data using advanced piloted maneuvers and fuzzy logic. 2012. Citations on pages 43, 45, 46, 65, and 97.

CHANG, R. C. Fuzzy logic-based aerodynamic modeling with continuous differentiability. **Mathematical Problems in Engineering**, Hindawi, v. 2013, 2013. DOI: <https://doi.org/10.1155/2013/609769>. Citations on pages 41, 43, 44, 45, 85, and 90.

FOSSEN, T. I. Mathematical models for control of aircraft and satellites. **Department of Engineering Cybernetics Norwegian University of Science and Technology**, 2011. Citations on pages 54, 58, 60, 61, 85, and 88.

IGNATYEV, D. I.; KHRABROV, A. N. Neural network modeling of unsteady aerodynamic characteristics at high angles of attack. **Aerospace Science and Technology**, Elsevier, v. 41, p. 106–115, 2015. DOI: <https://doi.org/10.1016/j.ast.2014.12.017>. Citations on pages 39, 40, 41, 42, and 43.

JAFELICE, R. S. d. M. *et al.* Modelagem fuzzy para dinâmica de transferência de soropositivos para hiv em doença plenamente manifesta. [sn], 2003. Citations on pages 47, 49, and 50.

JANG, J.-S. Fuzzy controller design without domain experts. In: IEEE. **[1992 Proceedings] IEEE International Conference on Fuzzy Systems**. [S.l.], 1992. p. 289–296. DOI: <https://doi.org/10.1109/FUZZY.1992.258631>. Citations on pages 29, 41, 47, and 50.

PEREIRA, B. L. *et al.* Aplicação de sistemas neuro-fuzzy e evolução diferencial na modelagem e controle de veículo de duas rodas. Universidade Federal de Uberlândia, 2017. Citations on pages 47, 51, and 52.

PRESS, W. H.; TEUKOLSKY, S. A.; VETTERLING, W. T.; FLANNERY, B. P. **Numerical recipes 3rd edition: The art of scientific computing**. [S.l.]: Cambridge university press, 2007. Citation on page 68.

px4.io. **Pixhawk Wiring Quick Start**. 2019. <https://docs.px4.io/en/assembly/quick_start_pixhawk.html>, Last accessed on 2019-05-24. Citation on page 66.

RAJKUMAR, T.; BARDINA, J. E. Prediction of aerodynamic coefficients using neural networks for sparse data. In: **FLAIRS Conference**. [S.l.: s.n.], 2002. p. 242–246. Citations on pages 34, 36, 37, and 38.

ROSKAM, J. **Airplane flight dynamics and automatic flight controls**. [S.l.]: DARcorporation, 1998. Citations on pages 36, 53, 54, 55, 56, 58, 75, and 86.

SECCO, N. R.; MATTOS, B. S. d. Artificial neural networks to predict aerodynamic coefficients of transport airplanes. **Aircraft Engineering and Aerospace Technology**, Emerald Publishing Limited, v. 89, n. 2, p. 211–230, 2017. DOI: <https://doi.org/10.1108/AEAT-05-2014-0069>. Citations on pages 36, 38, 39, and 40.

STORN, R.; PRICE, K. Differential evolution–a simple and efficient heuristic for global optimization over continuous spaces. **Journal of global optimization**, Springer, v. 11, n. 4, p. 341–359, 1997. DOI: <https://doi.org/10.1023/A:1008202821328>. Citation on page 52.

WANG, Q.; QIAN, W.; HE, K. Unsteady aerodynamic modeling at high angles of attack using support vector machines. **Chinese Journal of Aeronautics**, Elsevier, v. 28, n. 3, p. 659–668, 2015. DOI: <https://doi.org/10.1016/j.cja.2015.03.010>. Citations on pages 33 and 35.

XING, Y.; WANG, G.; ZHU, Y. Application of an autoregressive moving average approach in flight trajectory simulation. In: **AIAA Atmospheric Flight Mechanics Conference**. [S.l.: s.n.], 2016. p. 3846. DOI: <https://doi.org/10.2514/6.2016-3846>. Citations on pages 31, 32, and 33.